Measurement report: Source apportionment of volatile organic compounds at the remote high-altitude Maïdo observatory

Bert Verreyken[1,2,3], Crist Amelynck[1,2], Niels Schoon[1], Jean-François Müller[1], Jérôme Brioude[3],
Nicolas Kumps[1], Christian Hermans[1], Jean-Marc Metzger[4], and Trissevgeni Stavrakou[1]

[1]Royal Belgian Institute for Space Aeronomy, B-1180 Brussels
[2]Department of Chemistry, Ghent University, B-9000 Ghent, Belgium
[3]Laboratoire de l'Atmosphère et des Cyclones, UMR 8105, CNRS, Université de La Réunion, Météo France, 97744
Saint-Denis, France
[4]Observatoire des Sciences de l'Univers de La Réunion, UMS3365, CNRS, Université de La Réunion, Météo-France,
Saint-Denis, La Réunion, France

Correspondence: Bert Verreyken (bert.verreyken@aeronomie.be)

Abstract. We present a source apportionment study of a near-continuous 2-year dataset of volatile organic compounds (VOCs), recorded between October 2017 and November 2019 with a quadrupole-based high-sensitivity proton-transfer-reaction mass-spectrometry (hs-PTR-MS) instrument deployed at the Maïdo observatory (21.1°S, 55.4°E, 2,160 m altitude). The observatory is located on La Réunion island in the south-west Indian Ocean. We discuss seasonal and diel profiles of six key VOC species

5   unequivocally linked to specific sources — acetonitrile (CH_3CN), isoprene (C_5H_8), isoprene oxidation products (Iox), benzene (C_6H_6), C_8-aromatics (C_8H_{10}), and dimethyl sulfide (DMS). The data are analyzed using the positive matrix factorization (PMF) method and back-trajectory calculations based on the Lagrangian mesoscale transport model FLEXPART-AROME to identify the impact of different sources on air masses recorded at the observatory. As opposed to the biomass burning tracer CH_3CN, which does not exhibit a consistent diel variability, we identify pronounced diel profiles with a daytime maximum for

10   the biogenic (C_5H_8 and Iox) and anthropogenic (C_6H_6, C_8H_{10}) tracers. The marine tracer DMS generally displays a daytime maximum except for the austral winter when the difference between daytime and nighttime mixing ratios vanishes. Four factors were identified by the PMF: background/biomass burning, anthropogenic, primary biogenic and secondary biogenic. Despite human activity being concentrated in few coastal areas, the PMF results indicate that the anthropogenic source factor is the dominant contributor to the VOC load (38%), followed by the background/biomass burning source factor originating in the

15   free troposphere (33%), and by the primary (15%) and secondary biogenic sources (14%). FLEXPART-AROME simulations showed that the observatory was most sensitive to anthropogenic emissions west of Maïdo while the strongest biogenic contributions coincided with airmasses passing over the north-eastern part of La Réunion. At night, the observatory is often located in the free troposphere while during the day, the measurements are influenced by mesoscale sources. Interquartile ranges of nighttime 30-minute average concentrations of methanol (CH_3OH), CH_3CN, acetaldehyde (CH_3CHO), formic acid (HCOOH),

20   acetone (CH_3COCH_3), acetic acid (CH_3COOH) and methyl ethyl ketone (MEK), representative for the atmospheric composition of the free troposphere, were found to be 525–887 pptv, 79–110 pptv, 61–101 pptv, 172–335 pptv, 259–379 pptv, 64–164 and 11–21 pptv, respectively.

1   Introduction

25   Non-methane volatile organic compounds (NMVOCs) are key players in atmospheric chemistry. Their reaction with the main atmospheric oxidants modulates the oxidative capacity of the atmosphere (Zhao et al., 2019) and, in combination with NO_x, results in the production of tropospheric ozone (O_3) and secondary organic aerosol (SOA), both air pollutants affecting human health (Jerrett et al., 2009) and short-term climate forcers. Whereas increases in tropospheric O_3 contribute to global warming, SOA affects radiative forcing both through direct interaction with radiation and indirectly by acting as cloud condensation

30   nuclei (CCN), resulting in an overall cooling effect (IPCC, 2013). Besides pure hydrocarbon compounds, which are emitted in huge amounts at the global scale and mainly by terrestrial vegetation, an important NMVOC class is composed of oxygenated compounds (OVOCs). These OVOCs can be directly emitted to the atmosphere by multiple sources, including the biosphere (vegetation and soils), biomass burning, anthropogenic activities and the ocean. Secondary production by oxidation of primary emitted NMVOCs, however, is a very important and often badly quantified source for many OVOCs as well. Moreover, recent

35   research has pointed to the importance of bidirectional exchange of OVOCs with oceans (Yang et al., 2014) and terrestrial vegetation (Farmer and Riches, 2020), a process which is not well described in atmospheric models and which complicates OVOC budget calculations. In the absence of high concentrations of highly reactive non-methane hydrocarbons, OVOCs are expected to account for most of the OH reactivity in the remote tropical marine atmosphere (Travis et al., 2020). However, due to scarcity of observational constraints, OVOC sources and sinks are prone to large uncertainties in these regions (Millet

40   et al., 2010; Read et al., 2012; Travis et al., 2020). The OCTAVE project (https://octave.aeronomie.be, last access: 11 December 2020) aims at reducing those uncertainties through in situ measurements, satellite retrievals of global OVOC concentrations and tropospheric modelling. In the framework of this project, a quadrupole-based high-sensitivity proton-transfer-reaction mass-spectrometry VOC analyzer (hs-PTR-MS) was deployed for two years at the remote high-altitude Maïdo observatory (21.1°S, 55.4°E, 2,160 m altitude) at Réunion Island, a remote tropical French volcanic island in the south-west Indian Ocean. The

45   instrument continuously measured marine boundary layer air enriched with compounds originating from urbanized areas and ecosystems native to the island during the day. At night, the observatory is frequently located in or near the free troposphere. Part of this hs-PTR-MS dataset (April 2018), in combination with Aerolaser formaldehyde measurements, has already been used for formaldehyde source apportionment on the Island using positive matrix factorization (PMF) (Rocco et al., 2020). Another study focused on the detection of African biomass burning plumes during August 2018 and 2019 and their impact on

50   the (O)VOC composition at the Maïdo observatory (Verreyken et al., 2020).

The present study makes use of the complete dataset and aims at a better characterization of mesoscale (O)VOC sources by studying their seasonal, diel and inter-annual variability using PMF and back-trajectory calculations. Previous studies have described the mesoscale transport features over La Réunion and the impact on measurement campaigns taking place on the island (Lesouëf et al., 2011; Baray et al., 2013; Tulet et al., 2017; Guilpart et al., 2017; Foucart et al., 2018; Duflot et al.,

55   2019). The recent development of FLEXPART-AROME (Verreyken et al., 2019) — a Lagrangian transport model driven by

Year	Start	End	Duration	Type	Comments
2017	27 December	9 January	13 days	Tropical cyclone, Ava	Technical issues with the hs-PTR-MS instrument.
2018	9 January	20 January	11 days	Intense tropical cyclone, Berguitta	Maïdo closed
	1 March	6 March	5 days	Intense tropical cyclone, Dumazile	Maïdo closed
	13 March	20 March	7 days	Sever tropical storm, Eliakim	
	3 April	4 April	17 hours	Volcanic eruption	
	20 April	25 April	5 days	Tropical cyclone, Fakir	
	27 April	25 May	27 days	Volcanic eruption	Accompanied by occasional vegetation fires
	13 July	13 July	13 hours	Volcanic eruption	
	17 November	25 November	8 days	Social unrest due to the 'yellow vests' protests	Last 5 days had a partial curfew
2019	18 February	10 March	21 days	Volcanic eruption	
	10 June	13 June	54 hours	Volcanic eruption	
	29 July	30 July	24 hours	Volcanic eruption	
	11 August	15 August	4 days	Volcanic eruption	
	25 October	27 October	2 days	Volcanic Eruption	

Table 1. Periods of measurement interruptions and their causes during the two-year deployment of the hs-PTR-MS. Information from (Fournaise Info, 2018; Le Monde, 2018; Météo France, 2020).

meteorological data obtained from the operational mesoscale numerical weather prediction models used in the region by Météo France — provides the opportunity to study mesoscale transport and its impact on the near-continuous 2-year (O)VOC dataset recorded at the observatory. We start by describing the measurement site, the instruments, and the source attribution tools used in Section 2. We present the diel, seasonal and inter-annual variability of key tracers linked to known sources in Section 3.1.

60   This variability is discussed in light of sources identified by the PMF algorithm (Section 3.2) and back-trajectories calculated with FLEXPART-AROME (Section 3.3).
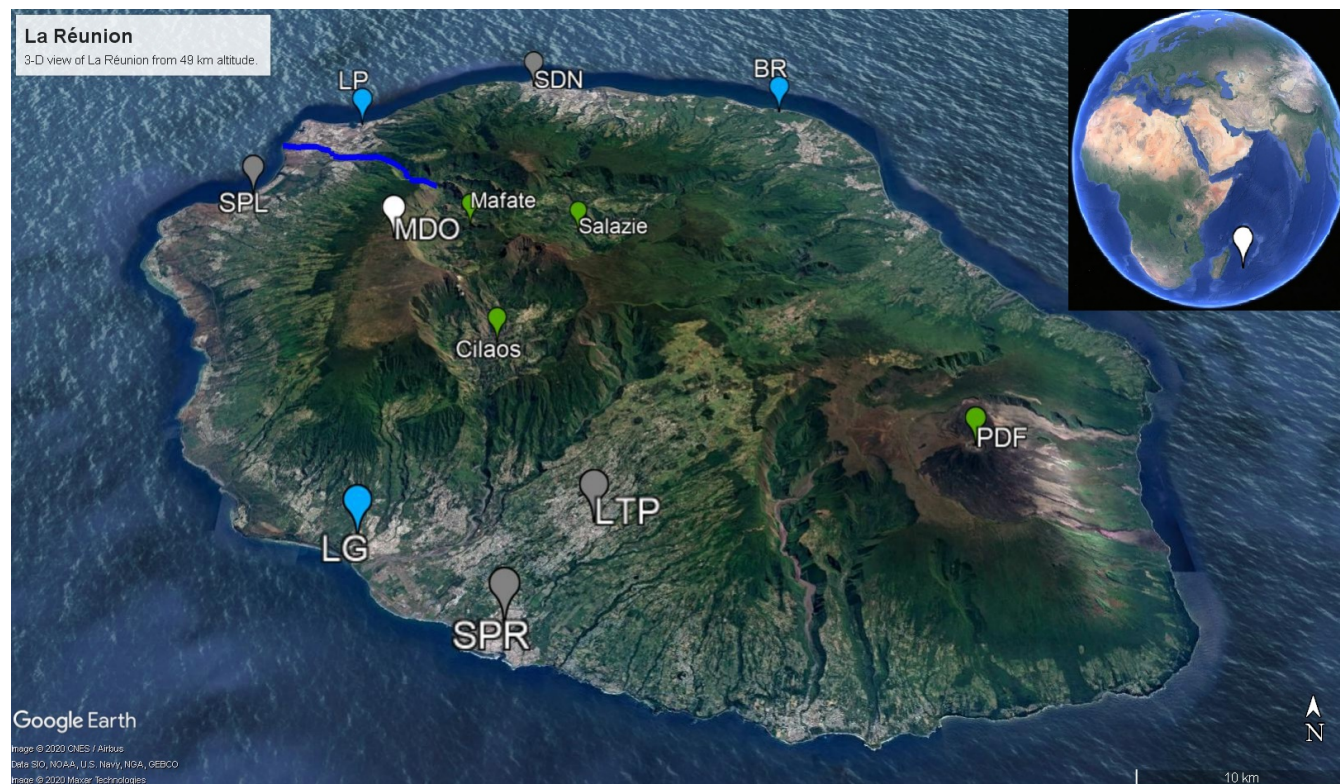
Figure 1. La Réunion, viewed from 49 km height. The Maïdo observatory (MDO) is indicated in white. Cities with population over 50,000 habitants — i.e. Saint-Denis (SDN), Saint-Paul (SPL), Le Tampon (LTP), and Saint-Pierre (SPR) — are shown in gray. The largest industrial sites — Le Port (LP), Bois-Rouge (BR), and Le Gol (LG) — are indicated in blue. Geological landmarks — Calderas Mafate, Salazie, and Cilaos as well as the shield volcano Piton de la Fournaise (PDF) — in green. The river Rivière des Galets between Mafate and Le Port is indicated as a dark blue line. Image generated with © Google Earth Pro, data SOI, NOAA, U.S. Navy, GA, GEBCO. ©2020 CNES/Airbus, ©2020 Maxar Technologies.

2 Materials and methods

2.1 Description of measurement site

La Réunion — a small tropical island located in the south-west Indian Ocean, shown in Figure 1 — is home to the high-altitude
65 Maïdo observatory (21.1°S, 55.4°E, 2,160 m altitude) (Baray et al., 2013). Despite urbanization of the coastal areas, the island still houses about 10,000 ha of native ecosystems (Duflot et al., 2019). The Maïdo observatory is located in a National Park and surrounded by mountain shrublands and heathlands (Duflot et al., 2019). The largest city is the capital, Saint-Denis. Other large cities (population over 50,000) are Saint-Paul, Saint-Pierre, and Le Tampon. Industrial emission hotspots at La Réunion are located near the power plants in Le Port (diesel power plant), Le Gol (biomass power plant), and Bois-Rouge (biomass
70 power plant). The island is home to the very active Piton de La Fournaise volcano (Tulet et al., 2017). La Réunion is isolated

from large landmasses and provides an ideal location to study complex processes and interactions in the remote atmosphere of anthropogenic, biogenic and volcanic emissions as illustrated by studies of e.g. volcanic plume emissions and ageing (Tulet et al., 2017), new particle formation (Foucart et al., 2018), and forest-gas-aerosol-cloud system interaction (Duflot et al., 2019). A recently published land-cover map of La Réunion (Dupuy et al., 2020) shows that a large fraction of the coastal zone

75   is used to cultivate sugar cane, which is by far the dominant agricultural crop, and fruit. While the eastern part of the island is mainly covered by woodlands. The western region is typically drier throughout the year and houses relatively more shrub and herbaceous savanna near the coast (Dupuy et al., 2020). Orographically-induced precipitation along the western mountain slope allows woodlands to be dominant at mid-level altitudes (Dupuy et al., 2020). There are two distinct seasons on the island, the warm and wet season (December to March) and the cold dry season (May to November) (Foucart et al., 2018). From October

80   to May, the region is sensitive to tropical cyclone activity. Synoptic scale air-mass transport in the region is dominated by east-south-easterly trade winds near the surface and westerlies in the free troposphere (FT) (Baldy et al., 1996; Lesouëf et al., 2011; Baray et al., 2013). These trade winds weaken from December to March but intensify from April to November (Baldy et al., 1996). The complex orographic profile of La Réunion (highest point over 3,000 m altitude) introduces a major obstacle in the stable wind flow pattern. Trade winds are split around the island with winds accelerating along the coastlines parallel

85   to the synoptic flow (Lesouëf et al., 2011). The northwestern area (lee side) of the island is sheltered from trade winds by the mountainous profile. Counter-flowing vortices in the wake of the island can trap polluted air masses (Lesouëf et al., 2011). Transport in the northwestern sector of the island is dominated by the coupling of sea (land)-breeze with upslope (downslope) transport during the day (night). During the day, the Maïdo observatory — located West of the Maïdo mountain peak — resides in the planetary boundary layer (PBL) while at night it is frequently in or near the FT (Lesouëf et al., 2011; Baray et al.,

90   2013; Guilpart et al., 2017; Duflot et al., 2019). During the day, a horizontal wind shear front located at the confluence of the mesoscale-driven upslope transport and overflowing trade winds determines air mass origins at the observatory (Duflot et al., 2019). When the front is west of the observatory, surface emissions have less impact on the composition of air masses as they originate mostly from 2,000 m altitude (Duflot et al., 2019). During the OCTAVE measurement period, several events occurred which could have affected in situ air mass composition and VOC mixing ratio diel profiles (tropical storms and cyclones,

95   volcanic eruptions). These are summarized in Table 1 but are not studied in detail as their effects are outside the scope of the current work.

2.2   Instrumentation and sampling setup

2.2.1   hs-PTR-MS

In October 2017, a high-sensitivity quadrupole-based proton-transfer-reaction mass-spectrometry instrument (hs-PTR-MS,

100   Ionicon Analytik GmbH, Austria) was deployed at the Maïdo observatory. It was run in multiple ion detection mode to generate a near-continuous dataset of (mostly) oxygenated volatile organic compounds from 19 October, 2017 to 26 November, 2019. The instrument was operated in H_3O^+ reactant ion mode at a drift tube pressure and temperature of 2.2 hPa and 333 K, respectively, and at a drift field of 600 V, which resulted in an E/N value (the ratio of the electric field to the number density in the drift

tube) of 136 Td. VOC-related product ion signals were sequentially recorded at mass-to-charge ratios (m/z) 31 (formaldehyde,
HCHO), 33 (methanol, CH_3OH), 42 (acetonitrile, CH_3CN), 45 (acetaldehyde, CH_3CHO), 47 (formic acid, HCOOH), 59 (ace-
tone, CH_3COCH_3), 61 (acetic acid, CH_3COOH), 63 (dimethylsulfide, DMS), 69 (isoprene, C_5H_8), 71 (methyl vinyl ketone,
MVK; methacrolein, MACR; and possible contributions from isoprene hydroxy hydroperoxides (Rivera-Rios et al., 2014),
ISOPOOH), 73 (methyl ethyl ketone, MEK), 79 (benzene, C_6H_6), 81 (sum of monoterpenes, $C_{10}H_{16}$), 93 (toluene, C_7H_8),
107 (C_8-aromatics, C_8H_{10}) and 137 ($C_{10}H_{16}$), each with a 10 s dwell time. In addition, ions at m/z 21 ($H_3^{18}O^+$), 32 (O_2^+) and
37 ($H_3O^+.H_2O$) were monitored with dwell times of 2s, 100 ms and 100 ms, respectively. A complete measurement cycle
lasted 2.7 min. Ion signals at m/z 31, 81 and 93 were not considered in the present analysis because of potential contributions
from interfering compounds or background values which were considerably larger than the minimum values in ambient air,
thus resulting in negative concentrations. It is well documented that hs-PTR-MS measurements of MVK+MACR (m/z = 71)
include contributions from ISOPOOH through the formation of MVK or MACR from ISOPOOH in the instrument (Liu et al.,
2013; Rivera-Rios et al., 2014; Bernhammer et al., 2017). As ISOPOOH is the major first-generation oxidation product of
C_5H_8 in low nitrogen oxides ($NO_x=NO+NO_2$) environments (Wennberg et al., 2018), we expect that the MVK+MACR signal
could suffer from interference from ISOPOOH. Therefore, we will refer to ion signal at m/z 71 as isoprene oxidation products
or Iox. Air was sampled 2.86 m above the roof of the observatory (8.20 m above ground) and pumped towards the instrument
through a 10.35 m long 3/8 inch (inner diameter) perfluoralkoxy (PFA) Teflon sampling tube (Dyneon 6502T, Fluortechniek-
Deutschland, Germany) at a flow rate of 8 L min^{-1}. The sampling line was heated (5–10 degrees above ambient temperature)
and thermally insulated to prevent condensation. The sampled air was filtered for particles 2.48 m downstream the sampling
point by a polytetrafluoroethylene (PTFE) membrane filter (Zefluor, Pall laboratory, MI, USA) with a pore size of 2 μm. Part
of the sampled air was sent through a catalytic converter (type HPZA-3500, Parker Hannifin Corp., OH, USA) for zero-VOC
measurements, which took place every four hours and lasted 30 minutes of which only the last minutes were taken into ac-
count. Calibration of the hs-PTR-MS for the target VOCs was performed every 3-4 days by dynamically diluting a VOC/N_2
calibration mixture (Apel-Riemer Environmental Inc., FL, USA; stated accuracy of 5% (2σ) on the VOC mixing ratios) in zero
air. In April 2018 and March 2019, the instrument was also calibrated with a commercial gas calibration unit (GCU, Ionicon
Analytik GmbH, Austria) from LSCE (Laboratoire des Sciences du Climat et de l'Environment). Calibration factors for the
(O)VOCs of interest obtained with the two calibration systems were found to be in excellent agreement. Calibration factors
for compounds that were not present in the calibration mixture — i.e. HCOOH and CH_3COOH — were determined indirectly
as mentioned in (Verreyken et al., 2020). The humidity dependence of the calibration factors was determined approximately
every 2 months by controlling the humidity of the zero air with a dew point generator (LI-COR LI-610, NE, USA). The ion
signal at m/z 37 was used as a proxy for air humidity. Of all compounds present in the calibration mixture, only the calibration
factors for formaldehyde, isoprene, Iox and MEK showed a non-negligible humidity dependence. The humidity dependence of
calibration factors for carboxylic acids – not present in the calibration mixture – was retrieved from (Baasandorj et al., 2015).

2.2.2 Additional measurements

The Maïdo observatory has recently been officially registered as an ICOS (Integrated Carbon Observation System, https://www.icos-cp.eu/, last access: 7 January 2021) atmospheric measurement site and a GAW (Global Atmospheric Watch, https://public.wmo.int/en/programmes/global-atmosphere-watch-programme, last access 7 January 2021) station. In this capacity, the observatory continuously houses a suite of both in-situ and remote sensing instruments. A list of all regular measurements can be found online (https://osur.univ-reunion.fr/observations/osu-r-stations/opar/, last access: 11 December 2020). In this study we will focus on carbon monoxide (CO) mixing ratios taken by a PICARRO G2401 instrument (PICARRO Inc., CA, USA). We will use the CO data to better characterize the presence of biomass burning (BB) plumes at Maïdo. Auxiliary data (wind direction, ambient temperature and solar radiation) were recorded by a meteorological station.

2.3 Source attribution tools

2.3.1 Positive matrix factorization

Air composition was studied using the positive matrix factorization (PMF) multivariate receptor model software released by the United States Environmental Protection Agency (EPA), EPA PMF 5.0 (Norris et al., 2014). PMF is a popular tool in atmospheric source attribution studies (e.g., Rocco et al., 2020; Pernov et al., 2020). The mathematical principle behind the PMF algorithm is based on the decomposition of measurements (x_{ij}) in a linear combination of factor profiles (f_{kj}) and factor contributions (g_{ik}), and a residual (ϵ_{ij}):

$$x_{ij} = \sum_{k=1}^{p} g_{ik} \times f_{kj} + \epsilon_{ij}. \tag{1}$$

The indices i, j and k denote the measurement time, the measured compound and the selected factor respectively. The total number of factors (p) represents the number of sources affecting the dataset and is a hyperparameter, i.e. a parameter set by the analyser to optimize the solution, for the algorithm. The only mathematical constraint to solve this equation is that all factor contributions and profiles must be positive. As a result, atmospheric sinks are not taken explicitly into account when deconstructing the dataset. The equation is solved by minimizing the objective function Q:

$$Q = \sum_{i=1}^{n} \sum_{j=1}^{m} \left[\frac{\epsilon_{ij}}{u_{ij}} \right]^2, \tag{2}$$

where n is the total number of measurements, m is the number of species and u_{ij} is the uncertainty of a measurement. In total, there are three different calculations of the objective function. The first takes into account all the residuals (Q_{true}), the second excludes a number of data points that are identified by the software as outliers (Q_{robust}), and the last version of the objective function is equal to the difference between the number of data values that are characterized as 'strong' (see Section 3.2) and the number of parameters fitted by the model ($Q_{expected}$). The $Q_{expected}$ corresponds roughly to the number of degrees of

freedom for the algorithm. The number of factors is set by scanning the parameter space and looking for a shift in both the

165 $Q_{true}/Q_{expected}$ ratio — also called Q_{scaled} — and the maximum root mean square (RMS) of residuals for the different compounds as well as ensuring physical interpretability of the resulting factor profiles and contributions.

2.3.2 Back-trajectory modeling

The FLEXPART-AROME model, a limited domain version of the Lagrangian transport model FLEXPART (Stohl et al., 2005; Pisso et al., 2019), was developed to simulate mesoscale transport over the complex orographic profile of La Réunion (Ver-

170 reyken et al., 2019). The model is driven by meteorological data generated by AROME, the operational mesoscale numerical weather prediction (NWP) model with a 2.5 km horizontal resolution used in the region by Météo-France. FLEXPART-AROME was initially developed from FLEXPART-WRF (Brioude et al., 2013) to forecast the dispersion of a volcanic plume for the STRAP campaign in 2015 (Tulet et al., 2017). In order to ensure harmonized turbulent transport in the NWP and the offline transport model, turbulence in FLEXPART-AROME was adapted to be driven by the 3D turbulent kinetic energy fields

175 obtained from AROME (Verreyken et al., 2019). The FLEXPART-AROME model has been used to study impact of mesoscale transport on BB plumes from distant sources (Verreyken et al., 2020). The model is driven by combining AROME forecasts generated daily at 00:00, 06:00, 12:00 and 18:00 UT. From 3 November 2017 until 26 November 2019, 20,000 air parcels are initialized every hour between 0 and 20 m above ground level (a.g.l.) at 21.081 °S, 55.383 °E. The model is run in backward mode (Seibert and Frank, 2004). Air parcels are traced 24 hours backward in time and are separated in two age classes (ACs)

180 of 12 hours. Air parcels' residence times (RTs, expressed in seconds) are computed in a grid with 0.025° (about 2.5 km) horizontal resolution between 19.5°S – 22.5°S and 53.0°E – 58.0°E with 15 vertical layers of 50 m thickness below 500 m a.g.l, 500 m thickness up to 2,000 m a.g.l and 2 additional layers above (10 km and 24 km height). Output is generated at time l and contains the RTs, i.e. the accumulated time all particles were present in grid cell m between times l and $l-1$. The RT is proportional to the impact of the emission rate of a source located in grid cell m at time l on the measurement related to

185 the release of air parcels at the location of the observatory (receptor) in the model. This proportionality is quantified by the source-receptor relationship (SRR, also called emission sensitivity) of area m (source) at time l and is calculated by:

$$SRR_{lm} = \frac{RT_{lm}}{h}, \tag{3}$$

where h is the height of the surface layer at time l. In practice, this h cannot be higher than the PBL but may not be too shallow in order to be numerically robust (Seibert and Frank, 2004). Concentrations at the receptor site of a passive tracer X

190 (not produced or lost during transport) can be calculated by:

$$C_X = \sum_l \sum_m E_{X,lm} \times SRR_{lm}, \tag{4}$$

where $E_{X,lm}$ is the emission rate (expressed in g m^{-2} s^{-1}) of tracer X related to area m at time l. As the (O)VOC compounds recorded with the hs-PTR-MS instrument are generally reactive compounds, the SRR from back-trajectory calculations are compared to the more robust PMF source factor contribution temporal variations. In this work, we will use the mesoscale

195 boundary layer movement towards Maïdo using a minimal static PBL proxy used by (Lesouëf et al., 2011). They represented

the PBL using a 500 m a.g.l. layer capped at 1,000 m above sea level (a.s.l.) In order to resolve this capping, the higher vertical resolution below 500 m a.g.l. in the FLEXPART-AROME output is needed. By using the minimal PBL proxy we simulate the arrival of pollutants emitted into the boundary layer further away from the observatory. In order to quantify the impact of local emissions, a second PBL proxy which is not capped at 1000 m a.s.l. is used. Two approximations are applied here when using

200   the SRR. Firstly, we accumulate the RTs over the complete period air parcels are transported over the specific source area for each release. By doing this, we do not consider a time dependence of emissions rates at the source. Since the largest temporal variation in emission rates manifests itself between day and night, coincident with the shift from PBL to FT air masses arriving at the observatory, we do not expect this approximation to significantly affect the results. Secondly, we separate the grid cells into three categorical variables (mountain, urban and marine) to identify the chemical signature of emissions at the source. The

205   emission sensitivity to marine emissions is determined by air parcels located in the PBL proxy over the ocean. As urban areas are located near the coasts, generally with surface elevations below 500 m a.s.l., air parcels located in the PBL proxy over this region are categorized as sensitive to urban emissions. The remaining area is categorized as mountainous, with usually strong biogenic emissions during the day. Using the minimal PBL proxy by (Lesouëf et al., 2011), the emission sensitivity in the mountainous area is restricted to a small band of surface elevation between 500 and 950 m a.s.l. By changing to the constant

210   500 m a.g.l. layer as a PBL proxy, we will only change the SRR of mountainous areas. We will discuss both the capped — PBL proxy by (Lesouëf et al., 2011) — and uncapped — constant 500 m a.g.l. — mountain categories. In the following, discussion of the mountain category refers to the uncapped PBL proxy unless specified otherwise. By using the categorical variables we neglect possible hotspots of anthropogenic sources related to industry or large cities. The relatively coarse resolution of AROME (2.5×2.5 km^2) does not permit to resolve local transport features induced by the strong orographic profile of La

215   Réunion for individual measurements. As such, we will be using the model output to discuss median diel profiles and combine releases in the model to identify the impact of mesoscale transport on measurements at the Maïdo observatory.

3   Results and discussion

Due to the high altitude of the Maïdo observatory, it is primarily located in the free troposphere during the night. During the day, the pristine marine boundary layer air over the ocean is thermally driven towards the observatory by the sea breeze coupled

220   to upslope transport on the western side of the Island. This mesoscale transport is in competition with overflowing trade winds coming from the east. During the day, marine air masses pass over both anthropogenic and biogenic sources affecting the atmospheric composition. The dataset is split into nighttime — 22:00 until 05:00 LT — and daytime — 10:00 until 17:00 LT. As seen in Table 2, (O)VOC concentrations are generally higher during the day, except CH_3CN and DMS which present similar mixing ratios between nighttime and daytime. We will first describe and discuss the diel, seasonal and inter-annual variability

225   of tracers recorded with the hs-PTR-MS instrument (Section 3.1). Next, the PMF algorithm is used to attribute the atmospheric (O)VOC burden to specific sources (Section 3.2) which are identified by comparing temporal variations of the PMF source factor contributions to diel and inter-annual variability of the tracers reported in Section 3.1. Finally, the results obtained in Section 3.1 and Section 3.2 are compared to back-trajectory calculations performed with FLEXPART-AROME (Section 3.3)

Table 2. Interquartile range of 30-minute average (O)VOC mixing ratios (MR) recorded at the remote high-altitude Maïdo observatory during nighttime (22:00 – 05:00 LT, FT) and daytime (10:00 – 17:00 LT, remote PBL). The last column indicates the median 30-minute average mixing ratio during nighttime with the standard deviation between parentheses. If the limit is below the limit of detection (LoD), we put < LoD.

Compound	Daytime MR [pptv]	Nighttime MR [pptv]	Nighttime median MR (σ) [pptv]
CH$_3$OH	990–1,531	525–887	724 (228)
CH$_3$CN	84–109	79–110	94 (39)
CH$_3$CHO	179–311	61–101	78 (41)
HCOOH	557–1,045	172–335	225 (474)
CH$_3$COCH$_3$	355–526	259–379	304 (152)
CH$_3$COOH	248–511	64–164	99 (226)
DMS	11–20	7–16	11 (7)
C$_5$H$_8$	80–223	< 9	< 9
Iox	48–136	< 3–8	4 (11)
MEK	35–69	11–21	15 (10)
C$_6$H$_6$	12–25	4–11	6 (9)
C$_8$H$_{10}$	< 10–21	< 10	< 10
C$_{10}$H$_{16}$	< 16–24	< 16	<16

to further validate the PMF results and assess the impact of mesoscale transport on the atmospheric composition recorded at
230   Maïdo.

3.1 Diel, seasonal and inter-annual variability

Discussion on annual and diel variability is limited to a subset of VOCs — CH$_3$CN, C$_5$H$_8$, Iox, C$_6$H$_6$, C$_8$H$_{10}$, and DMS — of which the patterns can be unequivocally attributed to different sources – pyrogenic, primary biogenic, secondary biogenic, anthropogenic and marine respectively. To support this discussion we use Figures 2-7 where the daily average concentrations,
235   seasonal median diel profiles and wind-separated (easterly versus westerly winds) median diel profiles for the different species under consideration and several meteorological parameters are shown.

3.1.1 Acetonitrile

Biomass burning is the main source of CH$_3$CN in the atmosphere (de Gouw, 2003) and is often used as an indicator for BB plumes in atmospheric studies (e.g., Verreyken et al., 2020). Its sinks are reaction with the hydroxyl radical (OH) and uptake
240   by the ocean surface. Both processes are slow, resulting in a long average atmospheric lifetime of CH$_3$CN, 1.4 years (de Gouw, 2003). This not only allows transport from distance sources (e.g. BB events in Africa, Madagascar but also South-America and Malaysia (Duflot et al., 2010; Verreyken et al., 2020)) but also allows the compound to be well-mixed in the atmosphere.
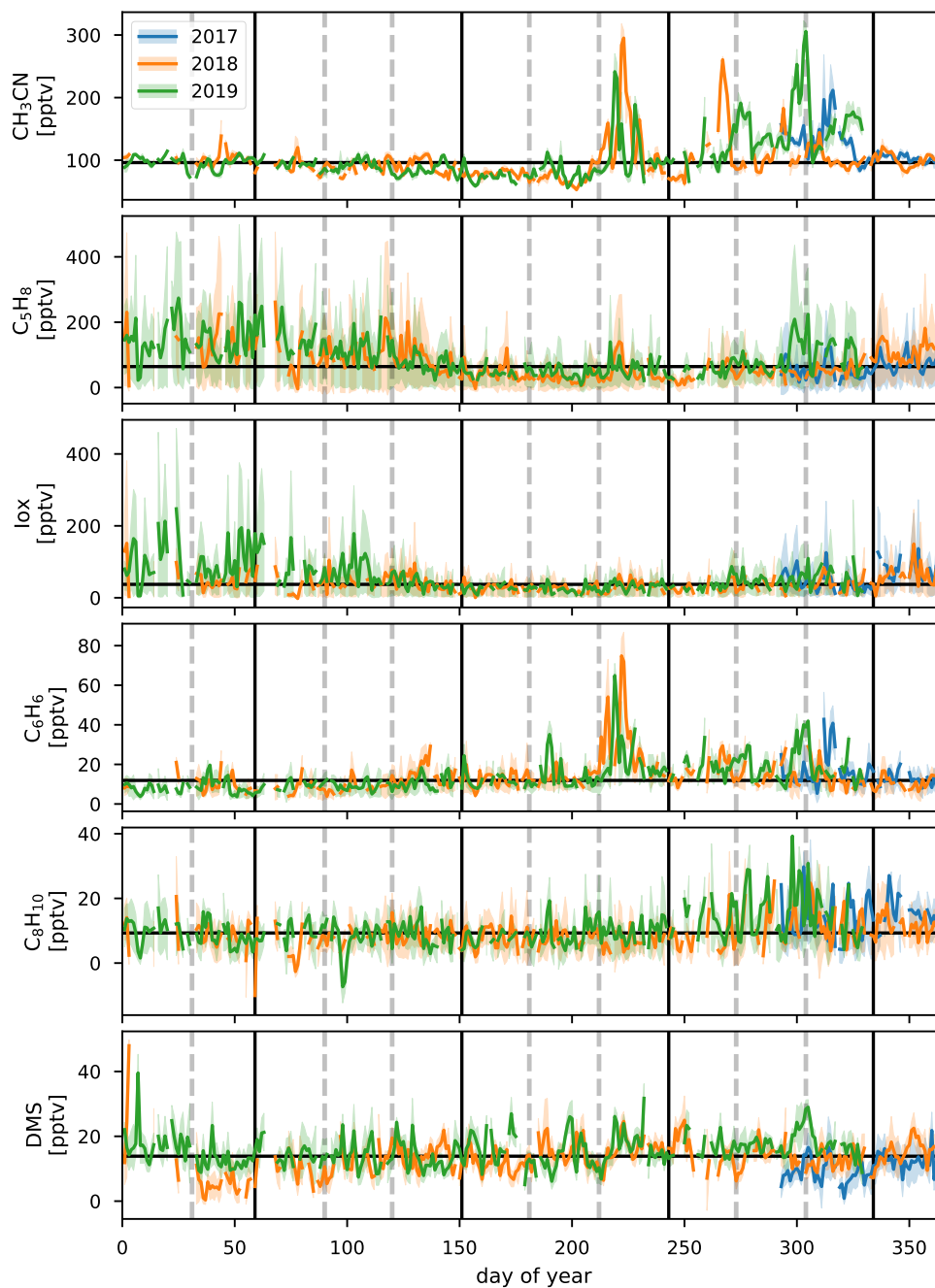
Figure 2. Daily average values of CH₃CN, C₅H₈, Iox, C₆H₆, C₈H₁₀, and DMS (top to bottom) for 2017, 2018, and 2019 (blue, orange and green respectively) during the deployment of the hs-PTR-MS instrument for the OCTAVE project. Shaded areas behind the curve show the diel interquartile range. Horizontal black line corresponds to the median daily average over the complete measurement period. Vertical gray dashed lines indicate the end of a month, vertical black lines separate the DJF, MAM, JJA and SON seasons.
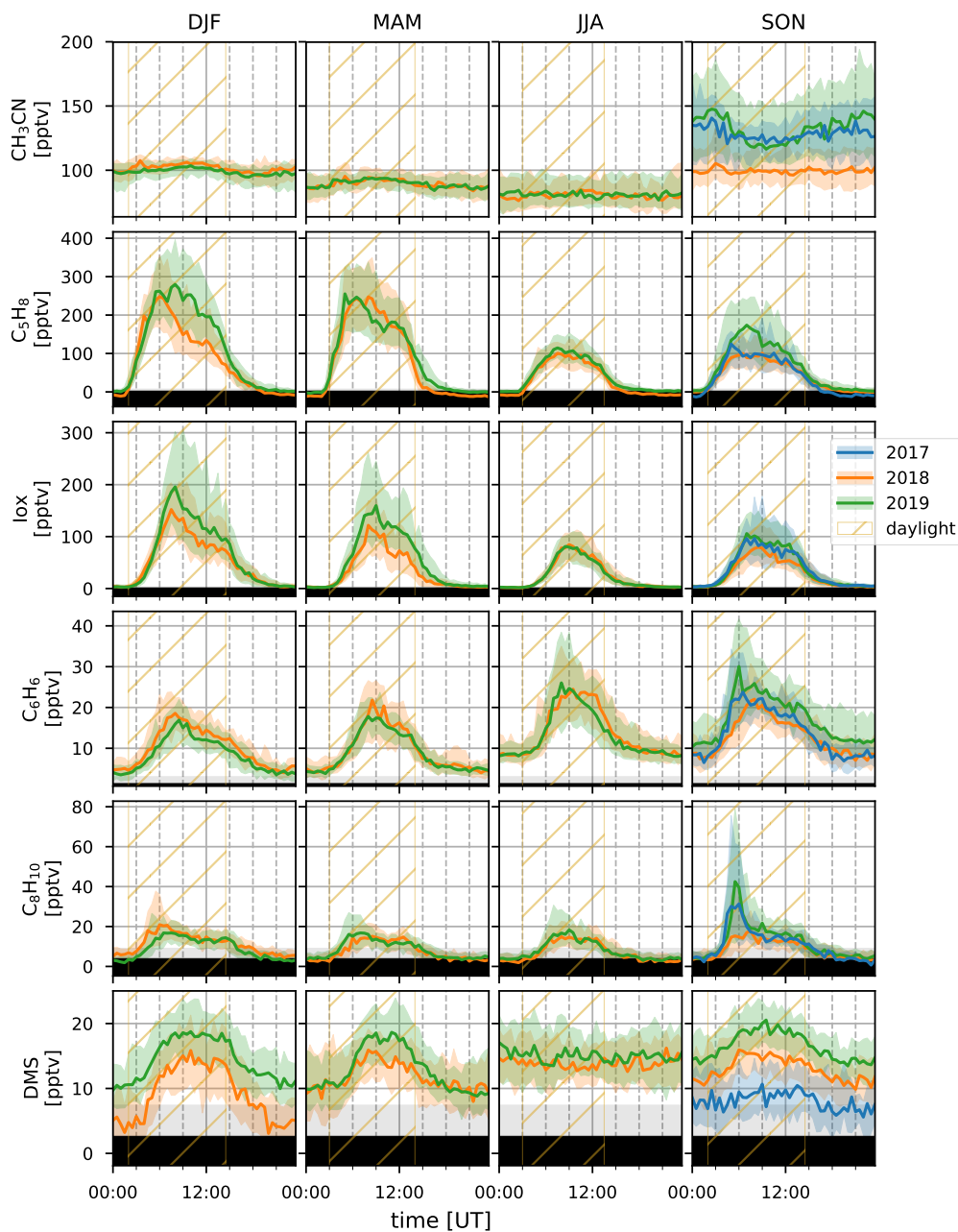
Figure 3. Median diel profiles (lines) and the interquartile distance (shaded area) for the DJF, MAM, JJA and SON seasons (columns, left to right) in 2017, 2018 and 2019 (blue, orange and green curves respectively) for CH$_3$CN, C$_5$H$_8$, Iox, C$_6$H$_6$, C$_8$H$_{10}$, and DMS (rows, top to bottom). The yellow hatched area illustrates daylight during the respective seasons. Gray background shows range between the median limit of detection and the minimum limit of detection of half-hour measurements. Individual half-hour measurements in the black region of the plots are not quantifiable.
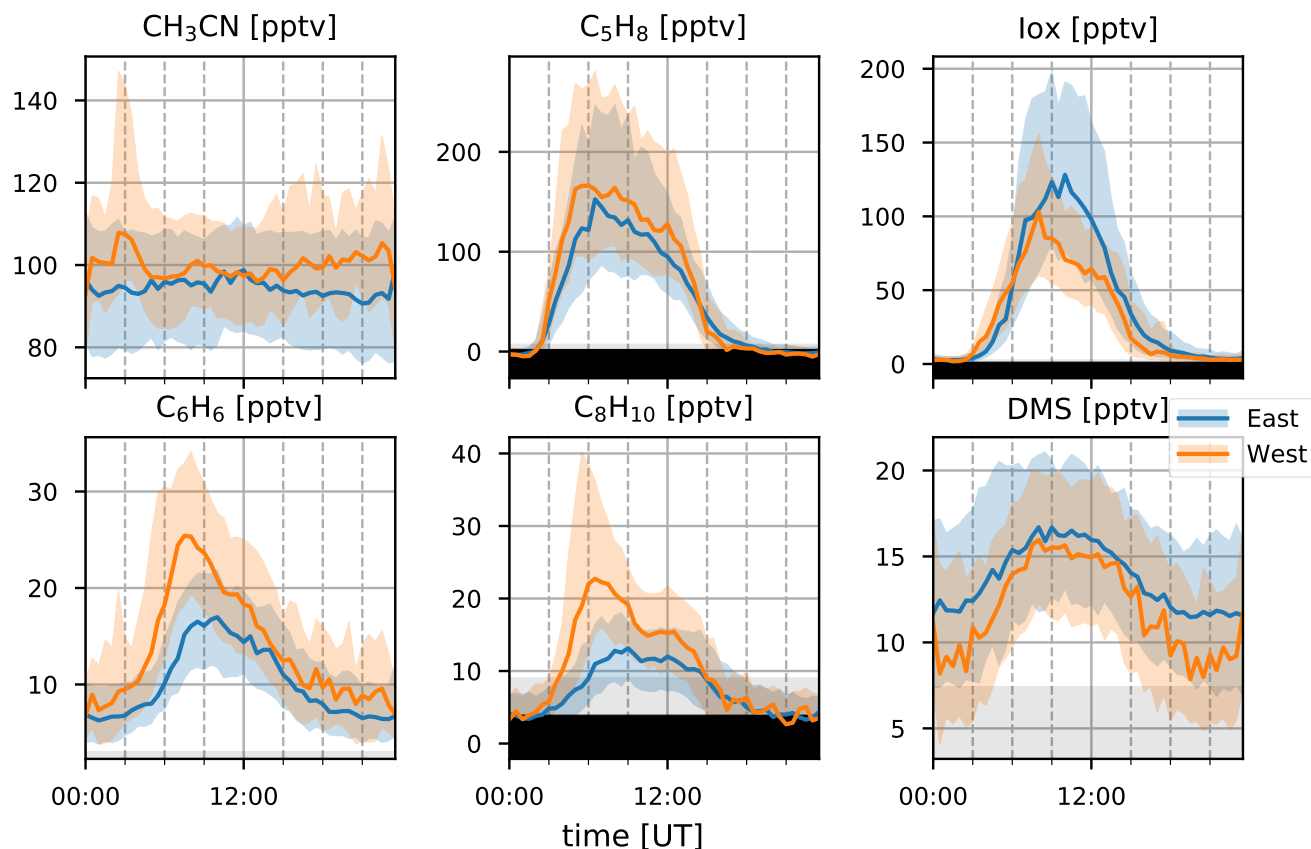
Figure 4. Median diel profiles (lines) and the interquartile distance (shaded area) for CH_3CN, C_5H_8, Iox, C_6H_6, C_8H_{10}, and DMS (top left to bottom right) separated between easterly (blue) and westerly (orange) transport recorded at the observatory. Gray background shows range between the median limit of detection and the minimum limit of detection of half-hour measurements. Individual half-hour measurements in the black region of the plots are not quantifiable.

From Figure 2 we see that high concentrations of CH_3CN occurred during August in both 2018 and 2019. This is due to direct transport of African BB plumes towards the Maïdo observatory (Verreyken et al., 2020). After these first intrusions,

245 the daily average mixing ratio is reduced to pre-BB plume intrusions (80–100 pptv). However, from September to November these daily averages are elevated (100–150 pptv) with spurious periods of high concentrations when BB plumes reach the observatory (up to 300 pptv). This period corresponds with the BB season identified from FTIR measurements at La Réunion (Vigouroux et al., 2012). The elevated daily averages drop to a minimum from March to August (50 pptv) after which the pattern repeats itself. The seasonal diel profiles (Figure 3) show no clear pattern except for the September-October-November

250 season (SON) of 2017 and 2019 where there is a nocturnal (nighttime maximum) signature. If we assume that CH_3CN is relatively well-mixed throughout the troposphere, this would suggest the existence of a marine sink. This was proposed from
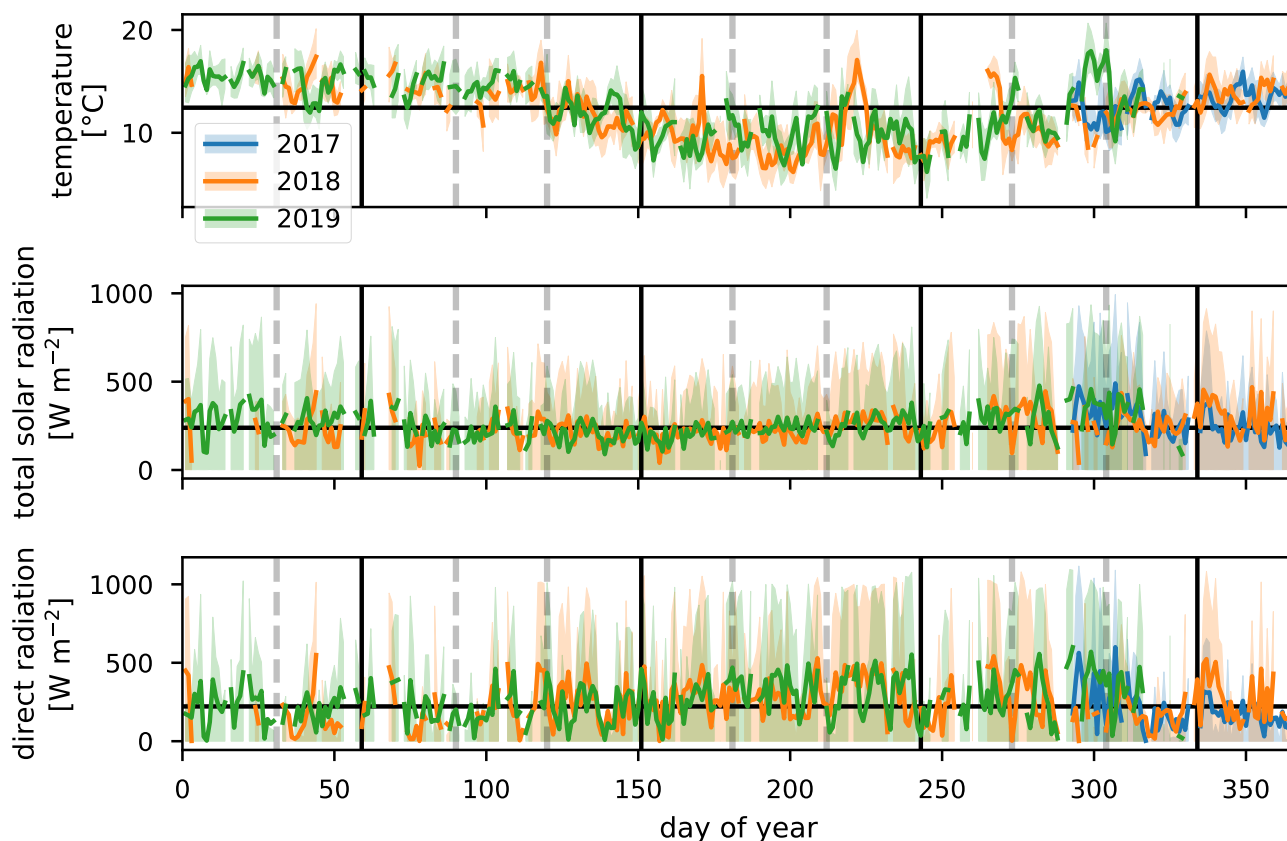
Figure 5. Daily average values of temperature, total solar radiation and direct radiation (top to bottom) for 2017, 2018, and 2019 (blue, orange and green respectively). Shaded areas behind the curve show the diel interquartile range. Horizontal black line corresponds to the median daily average over the complete measurement period. Vertical gray dashed lines indicate the end of a month, vertical black lines separate the DJF, MAM, JJA and SON seasons.

CH$_3$CN measurements at the Mauna Loa observatory in Hawaii (Karl et al., 2003). However, a study of BB plume transport of African and Madagascan pyrogenic emissions towards the Maïdo observatory found that these plumes are primarily transported through the FT (Verreyken et al., 2020). The median nocturnal pattern during the SON 2017 and 2019 seasons could likely be
255 due to the high number of plume days recorded during these periods. After the BB season (SON), the median diel profile is flat and its mixing ratio steadily drops from December-January-February (DJF, 100 pptv) to June-July-August (JJA, 80 pptv). The wind-separated profile of CH$_3$CN does not point to a difference in sources between the East or West (Figure 4).
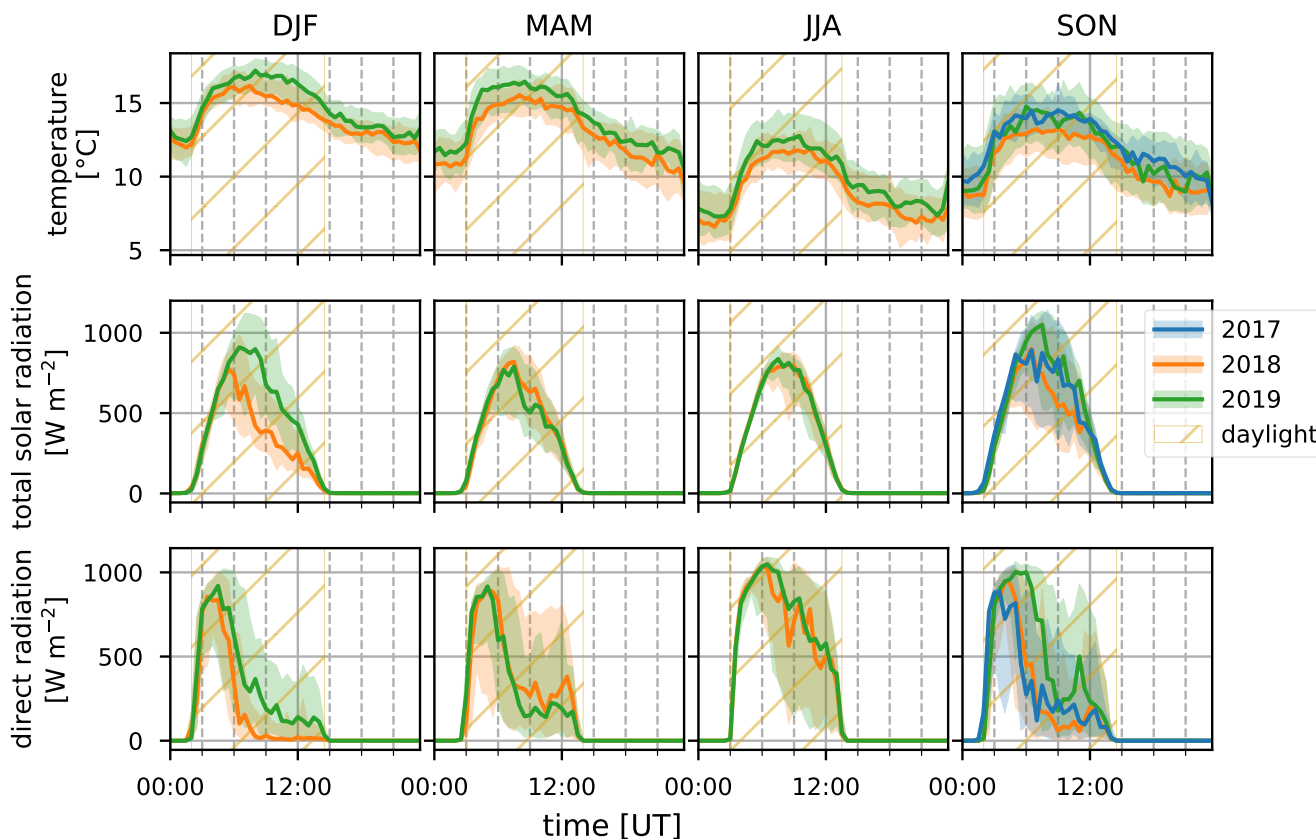
Figure 6. Median diel profiles (lines) and the interquartile distance (shaded area) for the DJF, MAM, JJA and SON seasons (columns, left to right) in 2017, 2018 and 2019 (blue, orange and green curves respectively) for temperature, total solar radiation and direct radiation (rows, top to bottom). The yellow hatched area illustrates daylight during the respective seasons.

3.1.2 Isoprene

Terrestrial biogenic emission of C_5H_8 strongly correlates to both temperature and solar radiation (Guenther et al., 1993).
260 Due to its short atmospheric lifetime, of the order of 1 hour (assuming an OH concentration of 2×10^6 molec. cm^{-3}), C_5H_8 mixing ratios at the observatory are largely due to emissions close to the observatory. The seasonal evolution of C_5H_8 displays low values in June—September and a gradual increase in the last months of the year (Figure 2). This relates closely to the annual temperature variation as measured at the Maïdo observatory (Figure 5). A clear diurnal (daytime maximum) pattern with mixing ratios increasing directly after sunrise (Figure 3) is observed. The 2018 DJF season has lower C_5H_8 mixing
265 ratios compared to the 2019 season. This pattern is also recorded for both the total solar radiation and the temperature during the same periods (Figure 6). The DJF 2018 and 2019 diel profiles (Figure 3) clearly illustrate the impact of the diel solar radiation and temperature profiles (Figure 6). Due to the much drier and less cloudy 2019, the DJF season profiles of the
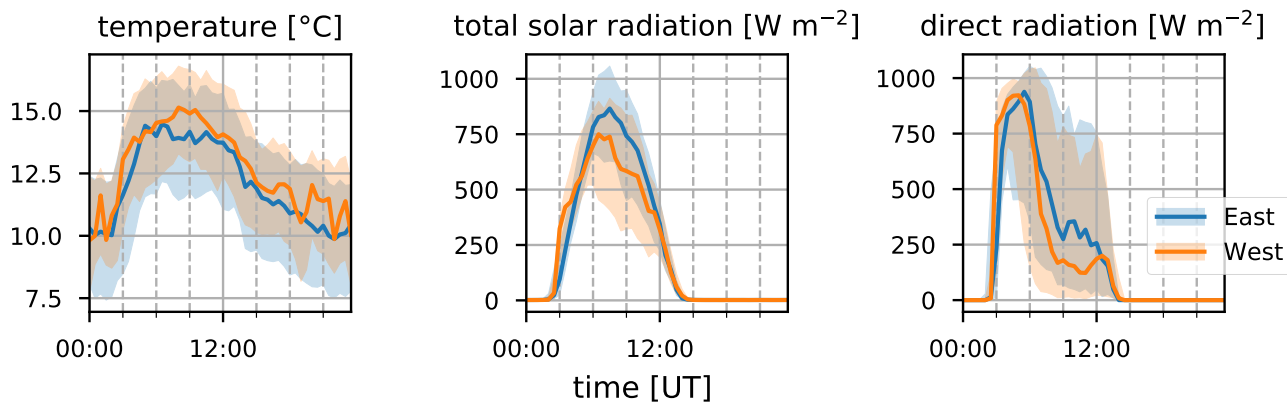
Figure 7. Median diel profiles (lines) and the interquartile distance (shaded area) for temperature, total solar radiation and direct radiation (left to right) separated between easterly (blue) and westerly (orange) transport recorded at the observatory.

relevant meteorological parameters and C_5H_8 mixing ratios are much more symmetrical than DJF 2018. The 2019 diurnal maximum during the SON season does not correspond with a maximum in temperature compared to other years (Figures 3 and 6) but it does relate to a maximum in measured total solar radiation. During the FARCE campaign (April 2015), it was found that mesoscale transport had a large role in the C_5H_8 mixing ratios recorded at the Maïdo observatory (Duflot et al., 2019). Easterly winds transported air masses originating mostly from 2,000 m a.s.l., thereby reducing the impact of surface emissions. Westerly winds are the result of thermally driven mesoscale transport and carry marine boundary layer (MBL) air masses over anthropogenic and biogenic sources towards the observatory. As such, westerly/easterly winds generally coincided with higher/lower C_5H_8 mixing ratios respectively. The difference in C_5H_8 concentration between the easterly and westerly flows were simulated with the non-hydrostatic mesoscale atmospheric model (Meso-NH) (Lac et al., 2018) during the FARCE campaign and were estimated to be ∼100 pptv (Duflot et al., 2019). When separating the C_5H_8 mixing ratios over the entire dataset of this study according to wind direction, we found that the median diurnal profile is indeed slightly more elevated when the wind is coming from the West compared to the East (Figure 4). The maximum difference in median diel profile between easterly and westerly regimes over the entire campaign is found to be 50 pptv. This takes into account the cold and dry season measurements where C_5H_8 mixing ratios are significantly lower than in April. Restricting our measurements to April 2018 and April 2019 (not shown) increases the discrepancy between wind regimes to a difference of 150 pptv with highest mixing ratios recorded from westerly transport. This is most likely related to the closer proximity of Maïdo to vegetation west of the observatory.

3.1.3 Isoprene oxidation products

As Iox generally have a longer lifetime than their precursor, their concentrations are a measure for the impact of biogenic sources further away from the observatory. The daily average variation of Iox (Figure 2) shows a similar signature as C_5H_8 with

high daily average mixing ratios recorded in the DJF and March-April-May (MAM, up to 250 pptv) seasons. The median diel profiles (Figure 3) show that the rise of Iox mixing ratios in the morning is delayed by about 1.5 h compared to C_5H_8, a duration

290   similar to the expected isoprene lifetime, when assuming an OH concentration of 2×10^6 molec. cm^{-3}. Contrary to C_5H_8, Iox are elevated in the easterly wind regime (Figure 4). This contradicts results from FARCE campaign which suggested that air masses transported by easterlies originate mostly from 2000 m a.s.l. with only limited impact of surface emissions (Duflot et al., 2019) as the discrepancy in Iox is generally larger than that of C_5H_8. The stronger Iox in easterly winds compared to the westerlies could be related to either a relatively stronger sink of C_5H_8 from easterly transport — either a more distant source

295   of C_5H_8 or elevated OH reactivity — or a larger source of C_5H_8 located to the East (either denser vegetation or larger area). Figure 7 shows that both total solar radiation and direct radiation are elevated when winds are coming from the east. This is due to reduced orographic cloud formation from the East which can enhance OH-formation through photolytic reactions and therefore accelerate the C_5H_8 sinks during easterly transport. It is however unlikely that increased production of Iox is the only possible source of the discrepancy as a similar difference in radiation is found between the MAM seasons from 2018 and 2019

300   (Figure 6). During MAM 2018, radiation at the observatory in the afternoon was slightly elevated compared to 2019, which could have enhanced the C_5H_8 sink and possibly Iox formation during MAM 2018 compared to 2019 (Figure 3). However, Iox signals during MAM 2019 were increased compared to 2018. From Meso-NH simulations performed in the context of the FARCE campaign, it was found that C_5H_8 concentrations in the morning (06:00 UT, 10:00 LT) are highest on the Northeastern part of the island (Duflot et al., 2019). The passage over this region of air masses arriving at the observatory from the East

305   could explain the discrepancy between wind regimes.

3.1.4   Benzene and C_8-aromatics

The seasonal variation of C_6H_6 is linked to BB (Figure 2). The excess C_6H_6 mixing ratios due to arrival of BB plumes in August 2018 and August 2019 have been studied in previous work (Verreyken et al., 2020). For C_8H_{10}, whose sources are mostly fugitive emissions from industry, car exhaust and volatilization through solvent use, this BB variability is not visible.

310   Not only are emission factors of C_8H_{10} at least 3 times smaller than those of C_6H_6 (Andreae, 2019), but the atmospheric lifetime of C_8H_{10} (hours) is much lower than that of C_6H_6 (weeks). C_8H_{10} is strongly enhanced during the SON seasons of 2017 and 2019. The median diel profiles of this season indicate that the SON mixing ratios of C_8H_{10} are enhanced in the morning (06:00 UT, 10:00 LT). This is most pronounced during the 2017 (maximum C_8H_{10} mixing ratio of 30 pptv) and 2019 (40 pptv) seasons. The median diel profile of C_6H_6 does show a slight elevation of mixing ratios at the same time as for C_8H_{10},

315   although it is less evident given the large amplitude of the regular diel profile seen in the other seasons. Comparison of the C_6H_6 and C_8H_{10} median diel profiles in westerly winds shows that the maximum in C_6H_6 occurs 1 hour after the peak in C_8H_{10} (Figure 4). The C_6H_6 median diel profile corresponds best with the diel profile of emissions related to energy production at La Réunion in the EDGAR database (Crippa et al., 2020) which has a large peak in the morning (05:00 UT, 09:00 LT) and slowly decreases towards the evening (16:00 UT, 20:00 LT) when it drops quickly. This in contrast to the median diel profile

320   of C_8H_{10} which correspond best with the two-peak profile of emissions from both residential and road traffic sources (Crippa et al., 2020).

3.1.5 Dimethyl sulfide

DMS is predominantly produced by marine phytoplankton and emitted in the atmosphere from the ocean surface. High regional abundances of DMS are linked to the presence of phytoplankton blooms in upwelling waters (e.g, Colomb et al., 2009). It has been reported that trees may also be a net source of DMS in the atmosphere (Jardine et al., 2015; Vettikkat et al., 2020). Globally, these terrestrial emissions are negligible (370–550 Mg DMS y^{-1} (Vettikkat et al., 2020)) compared to the estimated annual marine emissions (28 Tg S y^{-1}, which corresponds to 54.5 Tg DMS y^{-1} (Lana et al., 2011)). The main atmospheric sinks of DMS are daytime oxidation by OH, accounting for 73–84% of the total sink, and nighttime oxidation by the nitrate radical NO$_3$ (Berglen, 2004; Kloster et al., 2006). The global average atmospheric lifetime of DMS is 1.02–1.93 days (Berglen, 2004; Kloster et al., 2006). As La Réunion is located in the Tropics, the lifetime of DMS is expected to be shorter than the global average during the day (Blake et al., 1999). The DMS mixing ratios recorded at the Maïdo observatory are much lower (7–16 pptv in the FT during the night, 11–20 pptv in the planetary boundary layer during the day, Table 2) compared to reported measurements over the ocean (e.g. 60 ± 20 pptv from ship-borne measurements south of La Réunion, 24–30.2 °S, during the MANCHOT campaign in 2004). The lower mixing ratios are likely due to the near-absence of DMS sources over land in combination with oxidation by OH during daytime, when marine air can reach the observatory. At first sight, no clear seasonal pattern is visible (Figure 2). However, the diurnal maximum in DMS diel profiles during the SON, DJF and MAM seasons is not present during JJA (Figure 3). The nighttime values vary between years for the SON and DJF seasons, for reasons still unclear. The diel profiles separated according to the wind direction (Figure 4) suggest that westerly transport during the night is accompanied by somewhat lower mixing ratios (5–15 pptv) compared to easterly transport (8–16 pptv). Caution is required, however, as only few nighttime measurements were recorded with a westerly origin.

3.2 Source identification using positive matrix factorization

The source apportionment software EPA PMF v5.0 was used to attribute the variability of VOCs to their sources. The PMF is run using CO data in combination with CH$_3$OH, CH$_3$CN, CH$_3$CHO, CH$_3$COCH$_3$, CH$_3$COOH, C$_5$H$_8$, Iox, MEK, C$_6$H$_6$, C$_8$H$_{10}$ recorded with the hs-PTR-MS instrument. The 2.7-minute time resolved data from the hs-PTR-MS are accumulated over 1 h to match the temporal resolution of CO measurements and improve the signal-to-noise ratio (S/N) of the (O)VOC measurements. The mixing ratios are converted to mass concentrations [μg m^{-3}] for mass closure using local ambient temperature and pressure measurements. Data below the limit of detection (LoD) was set to LoD/2 with an associated uncertainty of $5/6 \times LoD$ in accordance with best practices (Norris et al., 2014). Measurements for which concentrations were missing for at least one of the species, were taken out of the dataset instead of replacing the missing information by an average value with high uncertainty. Data quality is quantified by using S/N. Species with low S/N ratio ($1.0 < S/N < 2.0$) were characterized as 'weak' (CH$_3$COOH) and corresponding uncertainties were multiplied by a factor of 3 (Norris et al., 2014). Species for which data was not available for the entire campaign (HCOOH) were excluded from the analysis. Additionally, DMS was not used in the PMF analysis, as preliminary tests indicated that including DMS would result in unexplainable factor profiles and contributions. Uncertainties are calculated using the displacement (DISP) and bootstrapping (BS) algorithms. Analysis of the complete
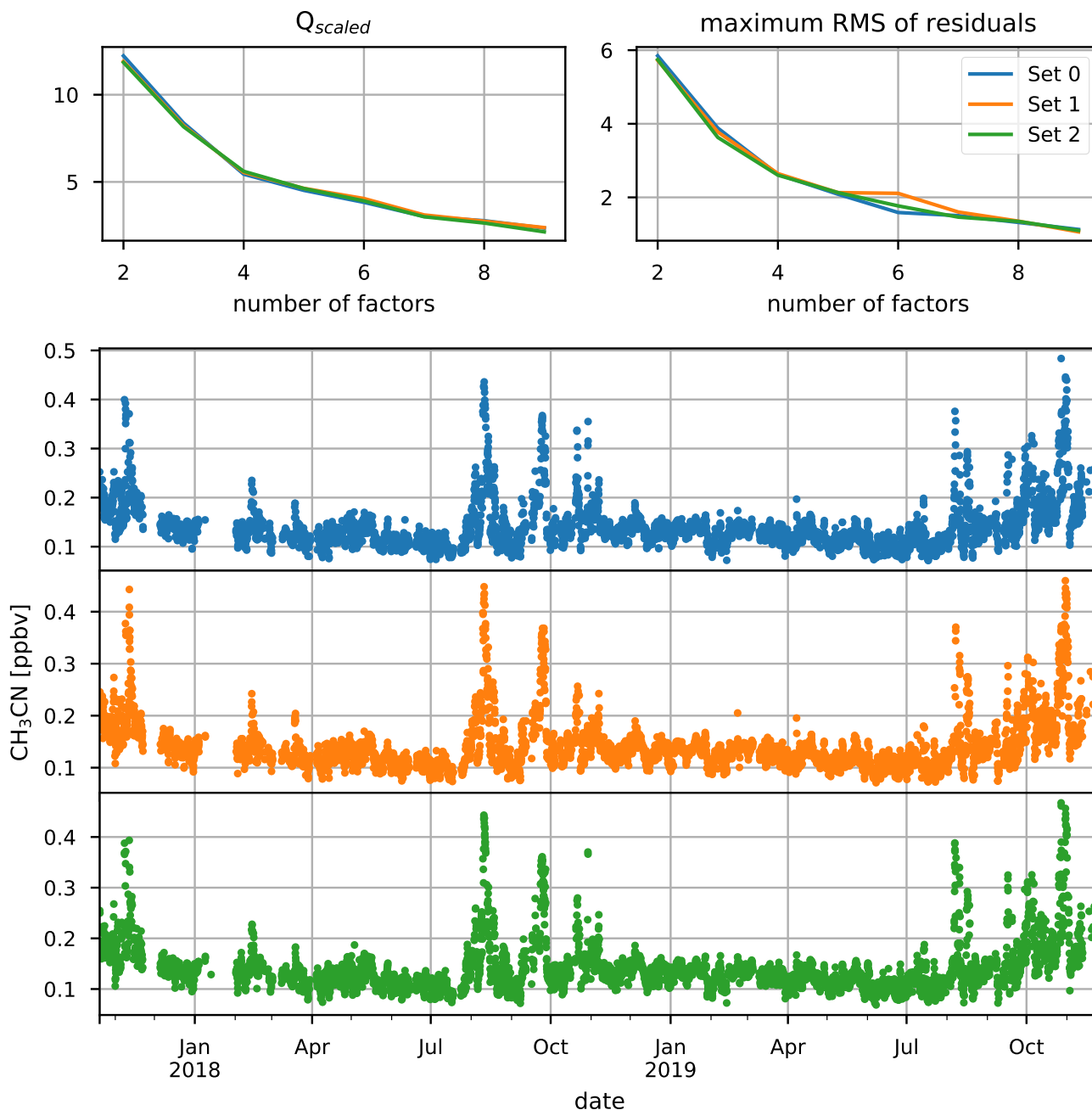
Figure 8. Dataset separation in three different subsets. The top two plots show the scaled objective function (left) and the maximal root mean square (RMS) of compound residuals (right) for a scan of the number of factor space from 2 to 9. The bottom three plots show the CH$_3$CN mixing ratios [ppbv] for the three different subsets which ensure near-equal occurrence of biomass burning intrusions.
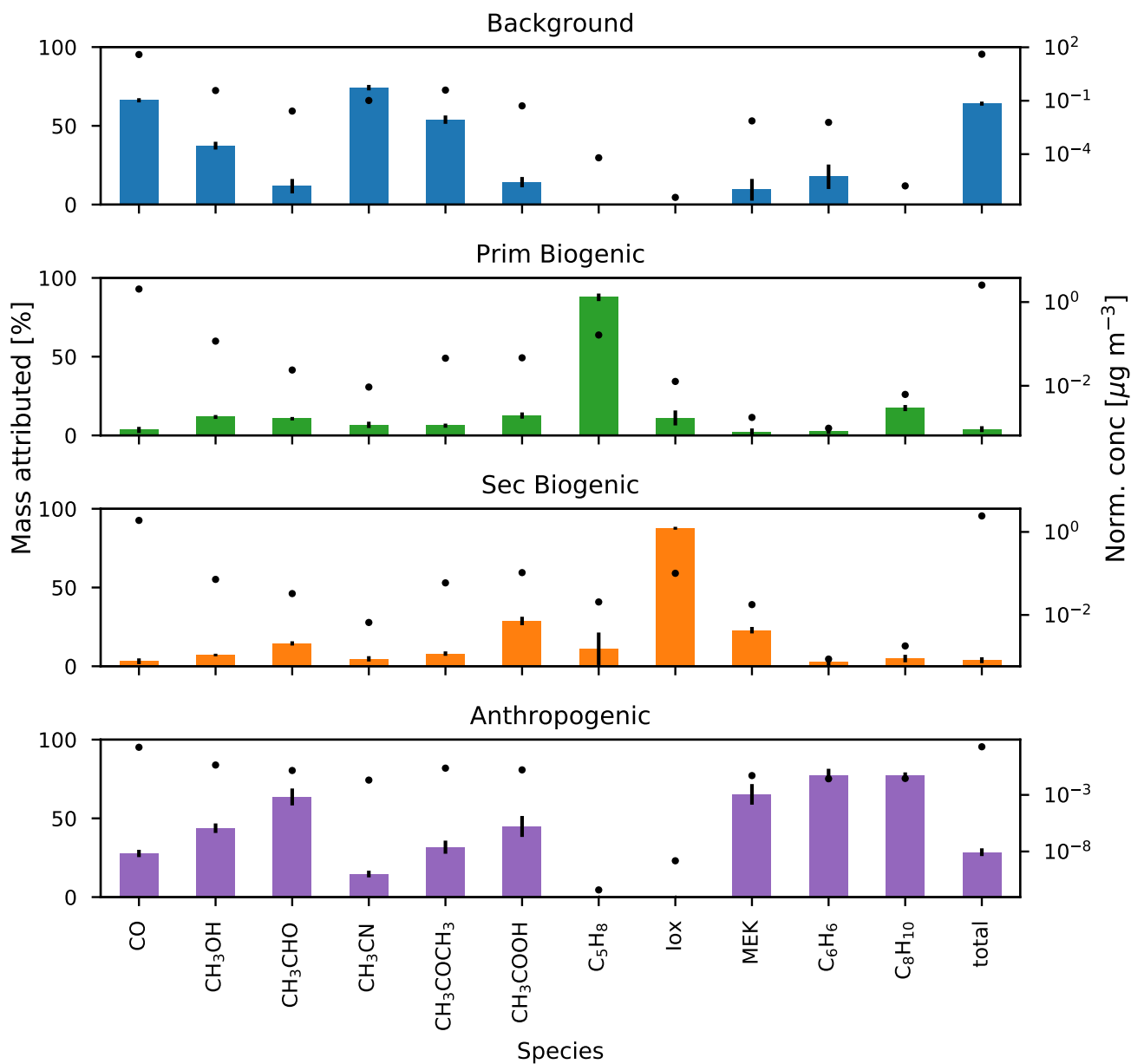
Figure 9. The median fraction of mass attributed [%] to the background, primary biogenic, secondary biogenic and anthropogenic factors calculated by the bootstrapping algorithm (bars, interquartile distance shown by error bars) and the median normalized concentration [μg m^{-3}] of the factor profiles (markers).
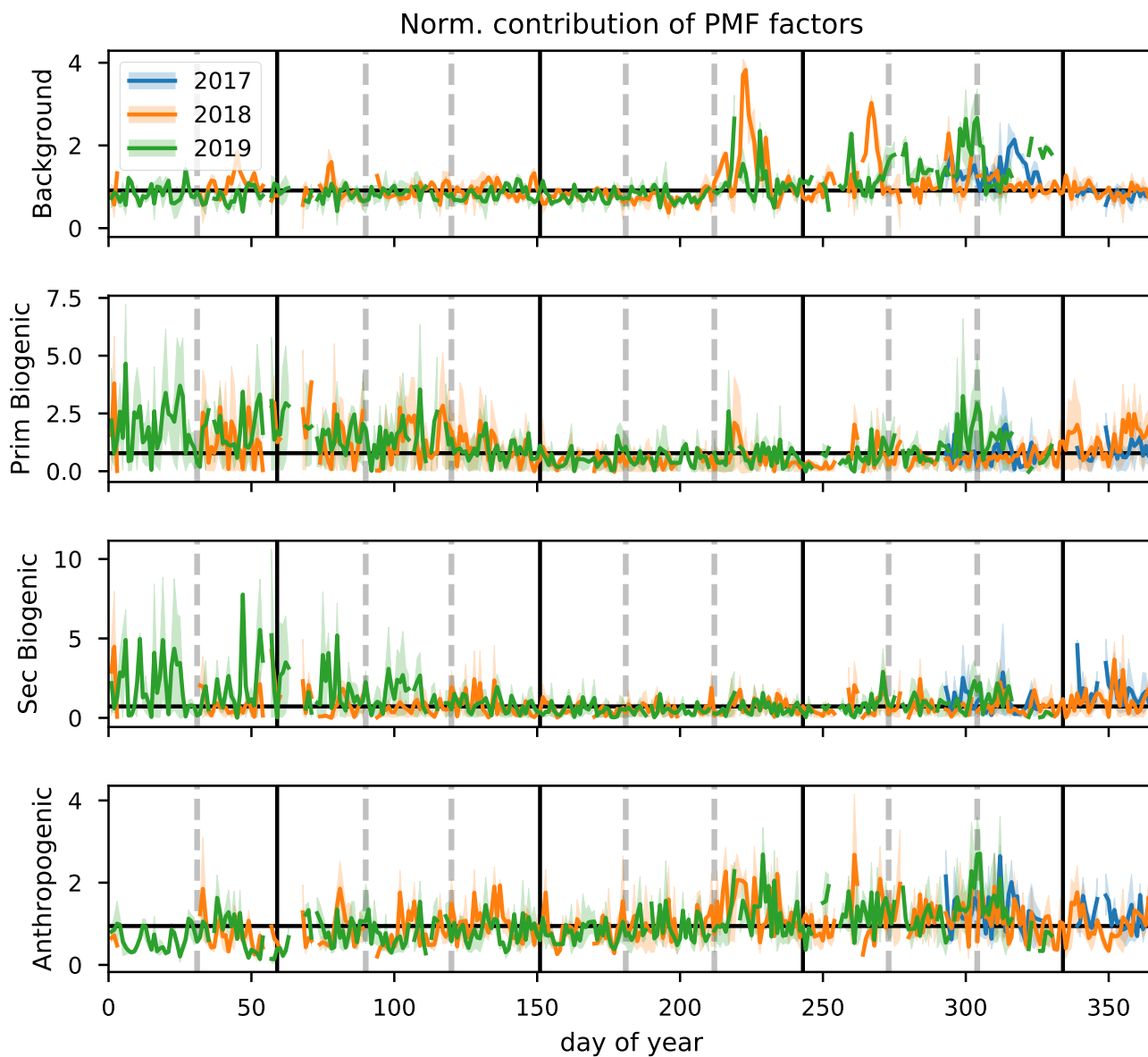
Figure 10. Daily average values of normalized contribution of the background, primary biogenic, secondary biogenic, and anthropogenic source factors (top to bottom) for 2017, 2018, and 2019 (blue, orange and green respectively). Shaded areas behind the curve show the diel interquartile range. Horizontal black line corresponds to the median daily average over the complete measurement period. Vertical gray dashed lines indicate the end of a month, vertical black lines separate the DJF, MAM, JJA and SON seasons.
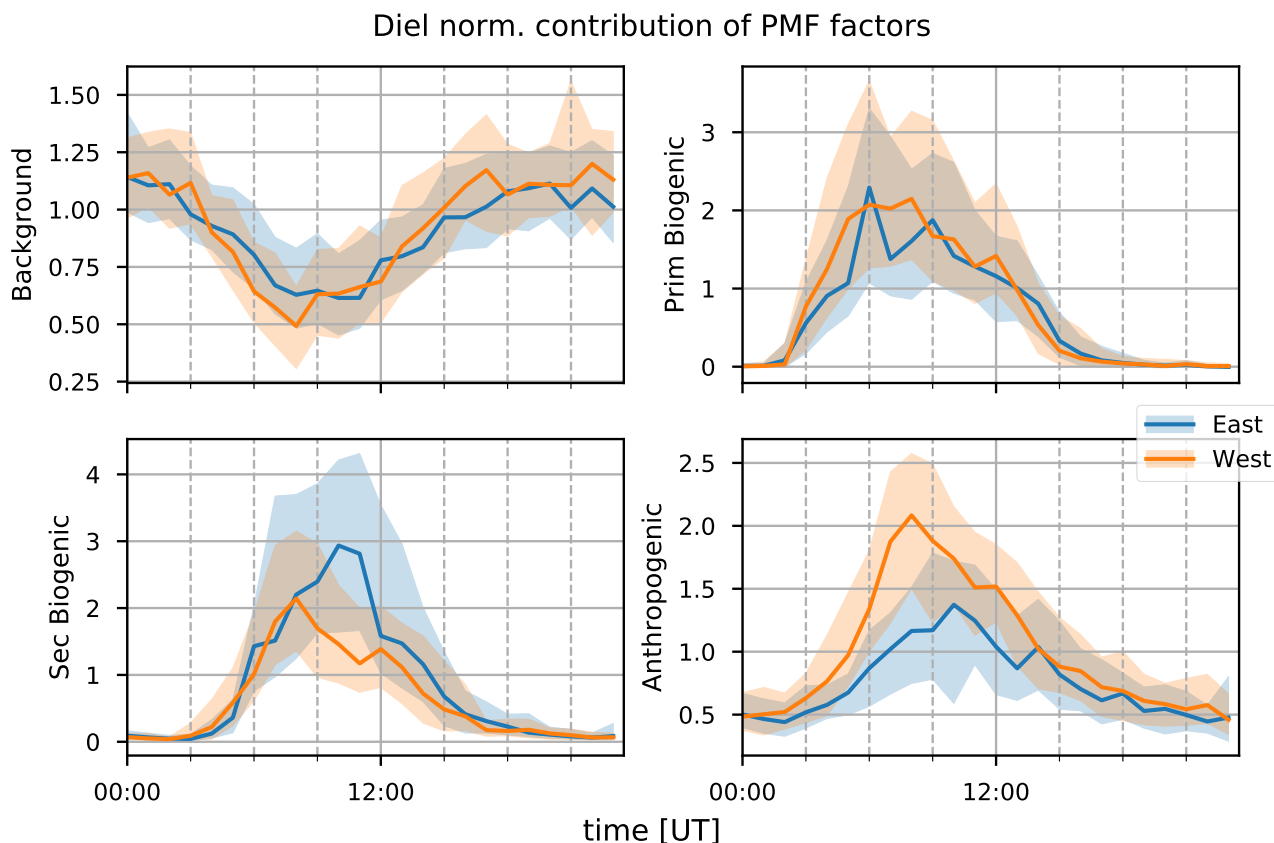
Figure 11. The median diel profile of background, primary biogenic, secondary biogenic and anthropogenic factor (top left to bottom right) normalized contributions separated along the wind directions recorded at the observatory (blue for eastern transport and orange for western transport), hourly interquartile distance is visualized by the shaded area.

355   2-year dataset by the EPA PMF 5.0 software was not possible as the dataset was too large. Instead, the dataset was randomly split up into three parts, while taking care to ensure equal contribution of BB intrusions in the three sets. This is checked using the temporal dataset of CH_3CN concentrations (Figure 8). Similar results for both the factor profiles and the contributions were obtained for all three subsets and we report here only the results for one of the subsets. After scanning the parameter space with 25 base runs for each number of factors, we selected the 4-, or 5-factor solution for further investigation based on the Q_{scaled}

360   and maximum RMS of residual curves (Figure 8). The base model was executed 100 times with a seed of 9 for both 4- and 5-factors. When using the DISP algorithm, no errors or swaps were reported using the 4- and 5-factor solutions, showing that they are free of rotational ambiguity. From the 100 BS run for the 4-factor solutions, it was found that 100% of the BS factors were mapped to the base run. This is not the case for the 5-factor solution (91%) which implies that, although still a robust solution, it is slightly more sensitive to random errors. However, the 5-factor solution had no straightforward interpretation

365 and was therefore discarded. A further investigation of rotational ambiguity of the 4-factor solution was performed using the F_{peak} functionality. This is used to investigate the effect of flattening (positive F_{peak} strengths) or sharpening (negative F_{peak} strengths) the factor contributions.. No decrease in the objective function was found using F_{peak} strengths of ±0.1, ±0.2, ±0.5, ±1.0, and ±2.0, which confirms that the 4-factor solution is free from rotational ambiguity. The four factors were identified as a background (which includes BB signatures), an anthropogenic, a primary biogenic, and a secondary biogenic factor. No

370 marine source was identified from the PMF algorithm in part due to the omission of DMS data from the analysis.

3.2.1 Background and biomass burning factor

The background and BB factor accounts for 65–68% of CO and 73–75% of CH_3CN measured at the observatory (Figure 9). This is a strong indication that the factor is indeed a combination of background and BB signals. The annual pattern of the normalized contributions (Figure 10) shows a strong influence of BB plumes reaching the observatory between August

375 and November. No other seasonal pattern is present. The median diel profile of normalized contributions (Figure 11) shows no influence of wind direction, which implies that the source is either near the observatory or remote. As the atmospheric lifetimes of both CO and CH_3CN are long, the source is identified as remote which is again in agreement with the identification of the factor as background/BB. The nighttime maximum of the normalized factor contributions suggests that it originates in the FT. It may also indicate the presence of an ocean sink of CH_3CN, as proposed by (Karl et al., 2003) and mentioned in Section 3.1.1,

380 which is obscured by a compensating mesoscale source of CH_3CN resulting in the recorded flat median diel profile. However, it seems unlikely that a mesoscale source would systematically compensate this atmospheric sink perfectly. We think it more likely that the PMF algorithm artificially reproduces the flat diel profile of CH_3CN (Figure 3) when it is well-mixed between the PBL and FT by attributing a small fraction of CH_3CN to other sources, inducing only small errors in the algorithm. The contribution of the background factor to the total mass of compounds included in PMF is 63–66%. This is strongly biased by

385 the high impact of CO concentrations that account for most of the mass of species included in PMF. Taking the contribution of CO out of the equation we find that the background factor accounts for 33% of the mass of (O)VOCs recorded at the observatory. The background factor is especially relevant for CH_3OH (30–39%) and CH_3COCH_3 (51–54%).

3.2.2 Anthropogenic factor

The anthropogenic factor accounts for 25–29%, 73–85%, and 75–79% of the mass of CO, C_6H_6 and C_8H_{10}, respectively

390 (Figure 9). This is a good indication that this factor is indeed related to anthropogenic sources. The seasonal variation (Figure 10) shows elevated normalized contributions in August-November. This may either be due to i) excess C_6H_6 present in younger BB plumes not represented in the background/BB factor (especially in August), or ii) the high C_8H_{10} mixing ratios in SON (Figure 2). The median diel pattern (Figure 11) shows a large impact from westerly transport, with a peak between 06:00 and 09:00 UT (10:00–13:00 LT), similar to C_6H_6 (Figure 4). This points to a strong influence of mesoscale transport on

395 the contribution of an anthropogenic source to the local atmospheric composition recorded at Maïdo. The difference in diel profiles between C_8H_{10} and C_6H_6 is not resolved by the PMF. Introduction of an additional factor did not result in a second anthropogenic source (e.g. by discriminating between combustion and evaporative sources as found at La Réunion during the

OCTAVE intensive observation period (IOP) (Rocco et al., 2020)). The anthropogenic factor accounts for 38% of the mass of (O)VOCs — i.e. excluding CO — recorded at the observatory. Besides C_6H_6 and C_8H_{10} mentioned above, the anthropogenic source is dominant for CH_3CHO (58–68%), CH_3OH (41–47%), CH_3COOH (38–51%), and MEK (57–73%), and is the second largest source for CO and CH_3COCH_3 (28–35%) for which the background is the dominant contributor.

3.2.3 Primary biogenic factor

The primary biogenic factor accounts for 85–94% of the mass of C_5H_8 recorded at the Maïdo observatory (Figure 9). Its normalized contribution (Figure 10) is enhanced during the hot and wet months (DJF and MAM). The median diel normalized contributions separated between wind regimes are found to be similar (Figure 11). Together with the short atmospheric lifetime of C_5H_8, this implies that the primary biogenic factor is mostly determined by emissions close to the observatory. The primary biogenic factor accounts for 15% of the mass of (O)VOCs recorded at the observatory. The primary biogenic source is the dominant source for C_5H_8 and the second largest source of C_8H_{10} (15–19%) and Iox (6–13%). The first is unexpected as C_8H_{10} is not usually associated with biogenic emissions. The latter probably accounts for a fraction of C_5H_8 emitted from local sources that is rapidly oxidized. This would have a large impact especially in the morning when C_5H_8 originating from emissions further away from the observatory cannot yet reach the observatory through mesoscale transport.

3.2.4 Secondary biogenic factor

The secondary biogenic factor accounts for 87–89% of the mass of Iox (Figure 9). The seasonal variation of the normalized contributions is similar to that of the primary biogenic factor (Figure 10). The median diel normalized contribution profile however shows a significant impact of wind direction (Figure 11). Similar to the diel profile of Iox (Figure 4), the normalized factor contributions are elevated in the easterly wind regime. This shows, similar to the anthropogenic source, a significant impact of sources on the island (further away from the observatory) to the secondary biogenic factor. The secondary biogenic factor accounts for 14% of the mass of (O)VOCs recorded at the observatory. It is the second strongest contributor for C_5H_8 (0–14%), MEK (21–26%), CH_3COOH (26–33%), and CH_3CHO (13–17%).

3.3 Source identification using FLEXPART-AROME back-trajectory calculations

The FLEXPART-AROME back-trajectory calculations showed that air masses are equally sensitive to mesoscale sources located on the island during the first 12 hours of the back-trajectory calculation compared to the complete 24 hours. The SRRs for the 24 hour trajectories had only significant impact on the marine category. The average total RT of air parcels in the first AC (12 hours backward in time) was 11.6 hours. This shows that a large fraction of air masses stayed within the domain during the first 12 hours of simulation. The average total RT of air parcels during the complete 24 hour back-trajectory calculation was 17.7, illustrating that a large fraction of air parcels is transported outside the FLEXPART-AROME output domain. We will therefore limit our discussion to SRRs calculated during the first 12 hours.
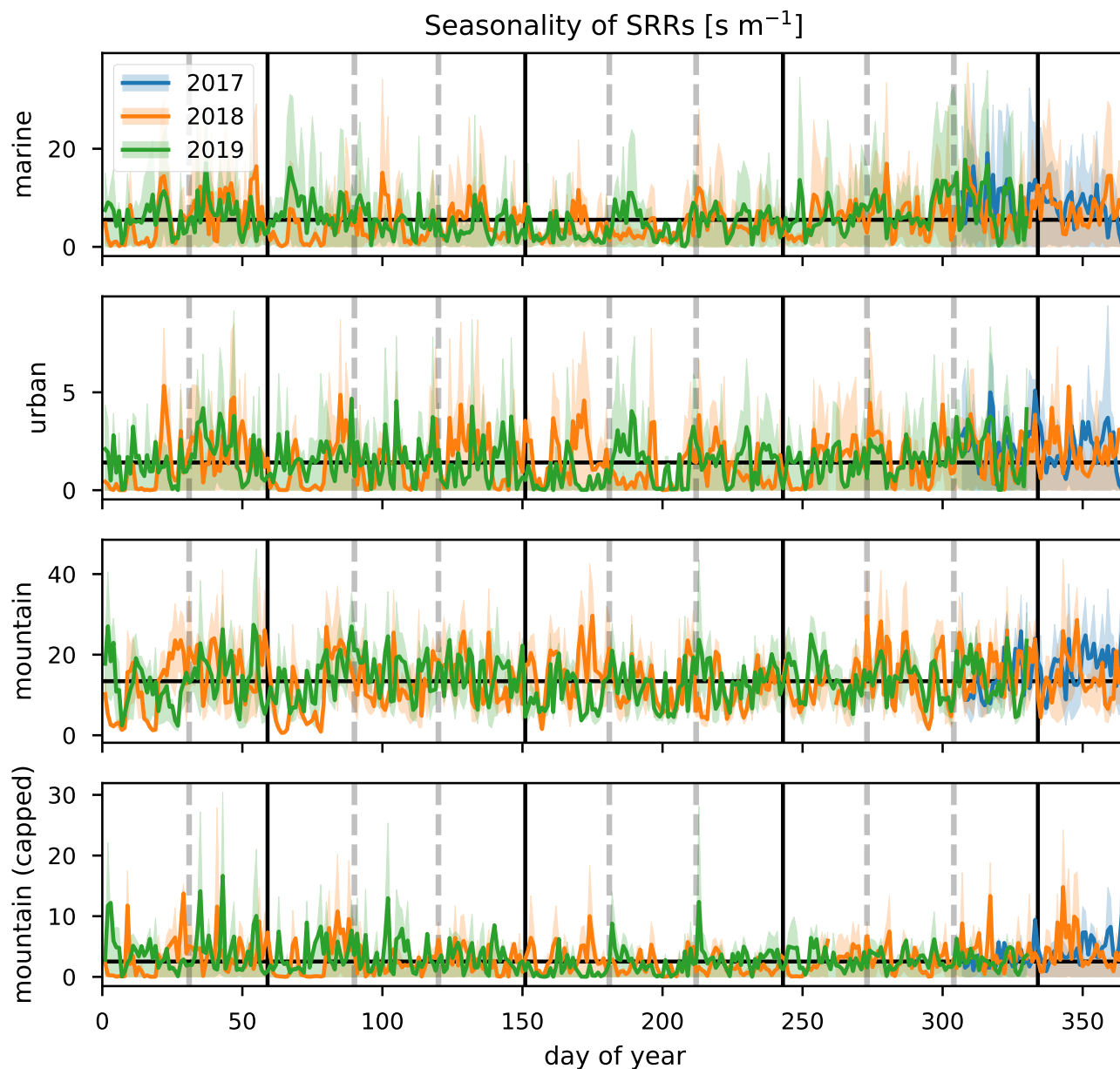
Figure 12. Daily average SRR [s m^{-1}] for marine, urban, mountain and capped mountain categories (top to bottom respectively) obtained from 12-hour FLEXPART-AROME back-trajectory calculations for the years 2017 (blue), 2018 (orange) and 2019 (green). Interquartile distance is shown as shaded area in the background.
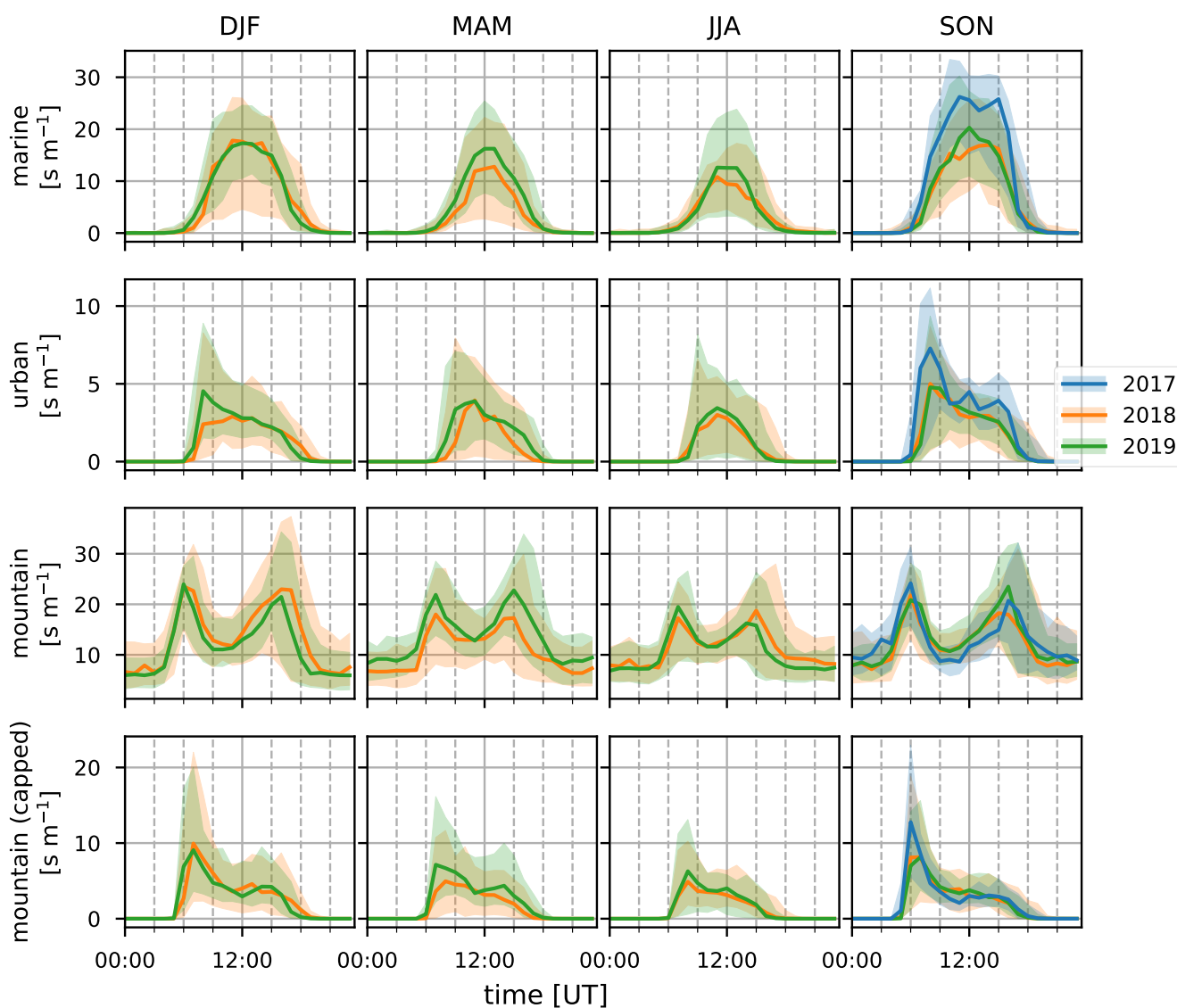
Figure 13. Median diel profile of the SRRs [s m^{-1}] calculated for the marine, urban, mountain and capped mountain categorical emission sources (columns top to bottom) with FLEXPART-AROME 12-hour back-trajectory calculations during the DJF, MAM, JJA and SON seasons (columns left to right) in 2017 (blue), 2018 (orange) and 2019 (green). The interquartile distances are shown as shaded areas.
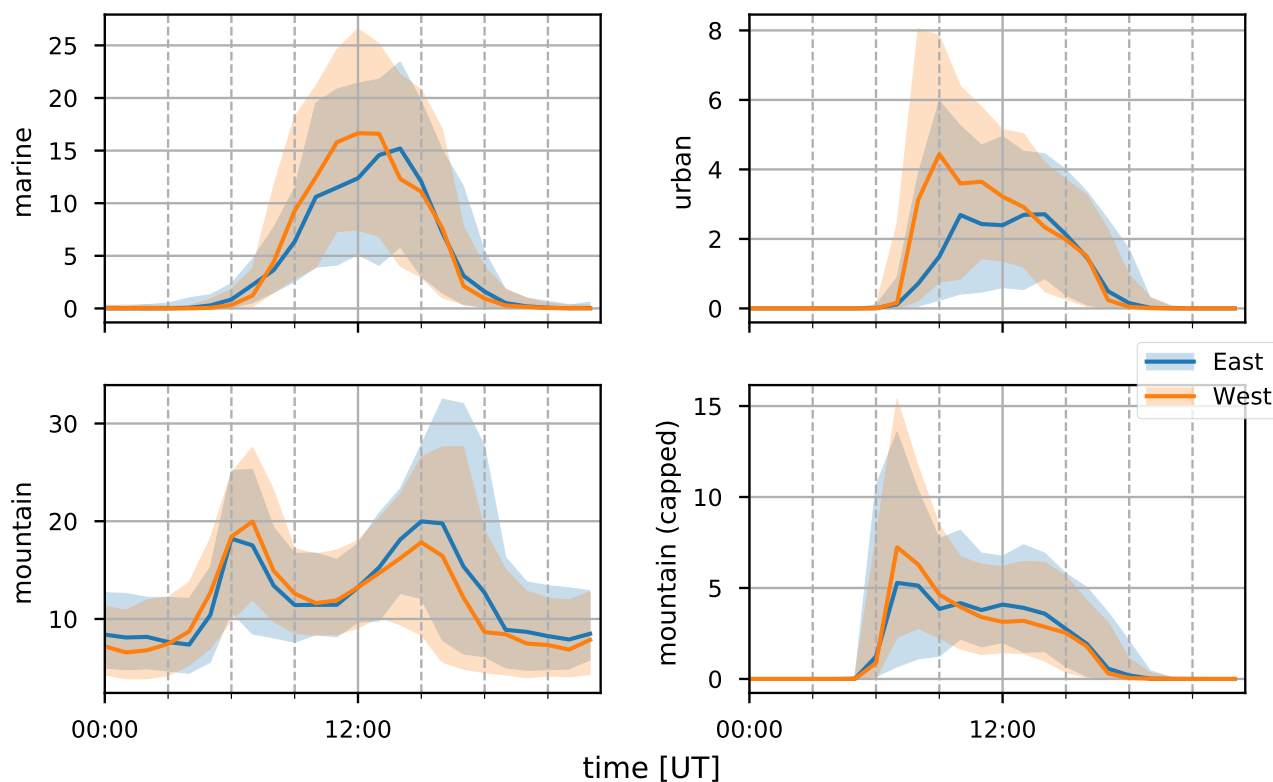
Figure 14. Wind-separated median diel profile (line) and interquartile distance (shaded area) for easterly (blue) and westerly (orange) transport for the marine (top left), urban (top right), mountain (bottom left) and capped mountain (bottom right) of categorical emission sources SRRs [s m^{-1}] as calculated using the FLEXPART-AROME 12-hour back-trajectory calculations. Wind direction separation based on measurements.

3.3.1 Diel, seasonal, and inter-annual variability

Figures 12 through 14 show the inter-annual daily averages, seasonal diel profiles and wind-separated diel profiles of the categorical SRRs. The daily average emission sensitivities for the different categories (Figure 12) do not show clear seasonal patterns for urban, and both capped and uncapped mountain emissions. The sensitivity to marine emissions is lowest during the JJA season (Figure 13). This is due to the strong trade winds during this time of year carrying air parcels outside the domain within the 12 hour period. The monthly average total RT in the first 12 hours is second lowest of all (11.1 hour). The month with lowest average RT (11.0 hour) is January due to the impact of tropical storms and cyclones (see Table 1). There are however clear seasonal differences when considering the median diel profiles shown in Figure 13. The urban SRRs profiles generally have a morning peak located at 07:00 UT (11:00 LT). This peak is less pronounced during the MAM period

and is not present during the JJA season. This may be due to the enhanced trade-winds together with a weakening of the thermally driven mesoscale transport during Austral winter resulting in overflowing easterly transport affecting the observations at the location of Maïdo more frequently. This is also what is seen in the wind-separated diel profiles (Figure 14) where the

440 easterly regime has a low sensitivity to urban emissions before 12:00 UT (16:00 LT) compared to westerly transport. The diel profile for urban SRRs does not show the morning peak in the DJF season of 2018. The strong winds associated to tropical cyclones and storms may be the cause during this season. The wind-separated marine SRRs (Figure 14) show stronger sensitivity from westerly transport between 07:00 UT and 13:00 UT (11:00–17:00 LT). This is counter intuitive as we assume that overflowing easterly transport is organized along faster winds and thus these air parcels spend less time over the island

445 which implies a relatively stronger impact of the ocean during the 12-hour back-trajectories. However, the amount of land to cross for these air masses is much larger. Moreover, air masses originating west of the observatory are conducted along the coast of La Réunion and may have been trapped over the ocean in the wake of the Island thus increasing the impact of marine emissions before being conducted towards the observatory through the coupled sea-breeze and upslope transport. The comparison between mountain emissions of the capped and uncapped categories manifests in two distinct features. Firstly,

450 the median diel profile of the uncapped mountain SRR never reduces to zero at night. This implies that, according to the FLEXPART-AROME backtrajectories, the Maïdo observatory always has an impact of mesoscale PBL emissions and never measures purely free tropospheric air masses. The lack of a zero baseline is due to the location of the receptor site within the static PBL proxy for the uncapped representation in the model. The second and most striking difference is the presence of the double peak in the uncapped PBL representation compared to the single peak profile for the capped version. The first peak

455 (present in both representations) is due to the reduced impact of the FT which is coincident with the onset of upslope transport. Afterwards the PBL is diluted as the boundary layer top rises in altitude, thus decreasing the emission sensitivity to mountain sources (both capped and uncapped). After sunset, radiative forcing becomes zero, resulting in a compression of the PBL and a decrease in upslope transport. The reduced upslope transport results in a reduction of emission sensitivities linked to the capped mountain category. The uncapped mountain category on the other hand does not depend on this mesoscale transport

460 and thus only shows the impact of the PBL compression which increases the S-R relationship before the PBL is flushed by the FT. Note that the wind-separated diel profiles for mountain emissions are not dependent on wind direction (Figure 14). This indicates that the discrepancy in the secondary biogenic source factor contribution between easterly and westerly flows (Figure 11) is not related to transport of mountainous air masses and originates from either i) a stronger oxidative sink of primary biogenic emissions, ii) air masses loaded with more biogenic emissions (denser vegetation/larger areas) or iii) a combination

465 of the above as discussed in Section 3.1.3. Here we can exclude the hypothesis of a larger source of biogenic emissions related to air masses passing over larger areas as this would be represented in the mountain SRRs.

3.3.2 Correspondence between FLEXPART-AROME and PMF

Table 3 shows the Pearson correlation coefficient (r) between the source-receptor relationship (SRR) of the different categories and the PMF source factor contributions. The correlations are generally low (maximum 0.45) due to the different approxima-

470 tions made in the categorization of SRRs and the neglected temporal variation of emission strengths, both diel and seasonal,
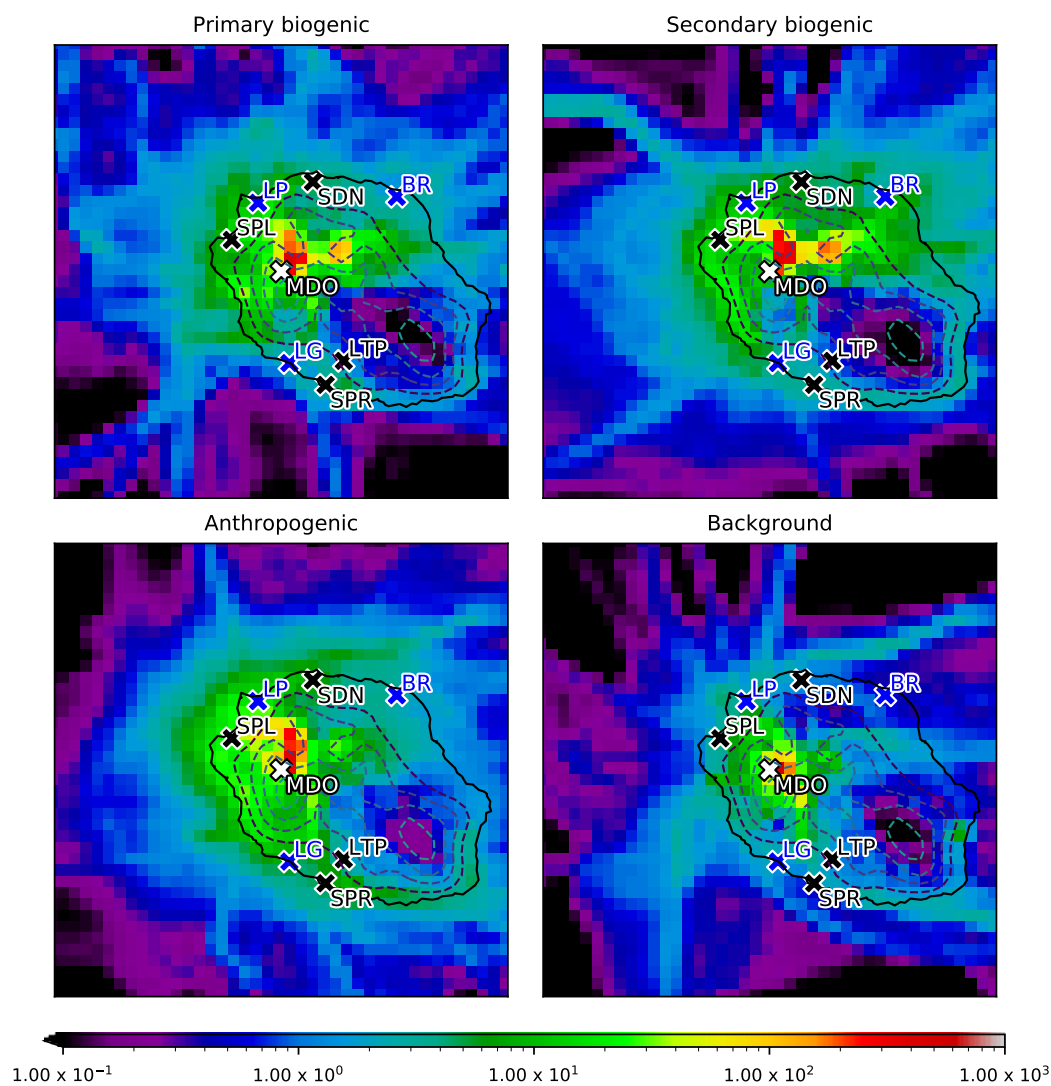
Figure 15. The spatial distribution of SRRs [s m^{-1}] over La Réunion for the top 5% source factor contributions calculated by the PMF algorithm for the primary biogenic (top left), secondary biogenic (top right), anthropogenic (bottom left) and background (bottom right) sources. The Maïdo observatory (MDO) is indicated in white. Cities with population over 50,000 habitants — i.e. Saint-Denis (SDN), Saint-Paul (SPL), Le Tampon (LTP), and Saint-Pierre (SPR) — are shown in black. The largest industrial sites — Le Port (LP), Bois-Rouge (BR), and Le Gol (LG) — are indicated in blue. Dashed lines are surface elevation contours in the FLEXPART-AROME model separated by 500 m.

Table 3. Pearson correlation coefficient (r) between categorical SRRs [m s^{-1}] and PMF normalized factor contribtuions.

r	Marine	Urban	Mountain (capped)	Mountain
Background	-0.08	-0.19	-0.25	-0.18
Anthropogenic	0.38	0.45	0.35	0.20
Primary biogenic	0.20	0.23	0.25	0.11
Secondary biogenic	0.36	0.36	0.40	0.20

at the source. The strongest correlation ($r = 0.45$) occurs between the urban SRR and the anthropogenic source contribution. This is due to the fact that the urban emissions have the most moderate seasonal profile. The low correlation is most likely due to the approximation of homogeneity of anthropogenic sources. The second highest correlation (0.40) is found between the secondary biogenic factor and the capped mountain source. It is expected that the capped mountain emission sensitivities

475 correspond better with the biogenic (both primary and secondary) sources than the uncapped category. This is because of the dependence of biogenic emissions on solar radiation which is not represented in the SRR. After sunset, the compression of the boundary layer results in a higher emission sensitivity from the uncapped mountain category. However, this increased sensitivity is compensated by a rapid decrease in biogenic emissions after sunset resulting in low mixing ratios of C_5H_8 (Figure 3) and low primary biogenic factor contributions (Figure 11). The better correlation of the SRR between the capped mountain

480 category and the secondary biogenic factor contributions (0.40) compared to that with the primary biogenic factor contributions (0.25) is due to the occurrence of primary biogenic emission directly after dawn near the observatory. The oxidation of C_5H_8 to Iox takes time, similar to transport of air masses from the capped PBL mountain category towards the Maïdo observatory. Figure 15 shows the spatial distribution of SRRs (i.e. not summed over the spatial index) also referred to as the field of view (Seibert and Frank, 2004) using the uncapped PBL proxy accumulated over the 5% largest source factor contributions from

485 PMF source factors. We note that the total surface sensitivity is smallest for the background factor (4.7×10^3 s m^{-1}), other total surface sensitivities are 7.2×10^3 s m^{-1}, 8.8×10^3 s m^{-1}, 9.1×10^3 s m^{-1} for the primary biogenic, anthropogenic, and secondary biogenic sources respectively). As discussed in Section 3.2.1, the background factor contributions are a combination of air transported predominantly in the FT and BB plume signals. As the BB plumes from Africa and Madagascar are mainly transported towards the Maïdo observatory through the FT (Verreyken et al., 2020), we expect the largest 5% factor contri-

490 butions to have a small SRR with mesoscale areas resolved from FLEXPART-AROME back-trajectories. From the similar median diel profiles of the wind-separated normalized factor contribution for the primary biogenic factor (Figure 11) we know that emissions are mostly located close to the observatory. However, from the C_5H_8 wind-separated profile (Figure 4), we see that there is a slight discrepancy with higher mixing ratios originating west of the observatory. This is contradicted somewhat by Figure 15 with a maximum east of the observatory. This location corresponds well with the region of highest C_5H_8 mixing

495 ratios modeled with Meso-NH during the 2015 FARCE campaign (Duflot et al., 2019). This biogenic emission hotspot is also visible in the field of view corresponding to the strongest secondary biogenic factor contributions where a strong impact of surface emissions is seen at the same location (Figure 15). A second feature in this map is the high impact north of the observatory

which diverts to the West towards Le Port and is then transported south. This transport is organized along the canyon of the river "Rivière des Galets" between Mafate and Le Port (Figure 1). The important role of river canyons with regard to pollutant

500   transport towards the Maïdo observatory has already been identified in the forward transport study using Meso-NH (Lesouëf et al., 2011). The field of view of the observatory related to the strongest anthropogenic factor contributions is highest west of the Maïdo observatory. The observatory is thus most sensitive to emissions from the industrial centers at Le Gol and Le Port and the second largest city Saint-Paul. Other emission hotspots of human activity did not contribute as strongly to the top 5% anthropogenic source factor contributions.

505   **4   Conclusions**

In this study, we analyzed the two-year dataset of (O)VOC concentrations obtained at Maïdo observatory between October 2017 and November 2019 in the framework of the OCTAVE project by a combination of i) diel, seasonal and inter-annual VOC concentration patterns, ii) a PMF algorithm and iii) the FLEXPART-AROME mesoscale transport model. The measurements are shown to be useful to characterize the atmospheric background composition, as evidenced by the high average impact of

510   the background/biomass burning source factor identified using the PMF algorithm on the atmospheric (O)VOC load (33%), which is even larger during the night. During the day however, the atmosphere is loaded with anthropogenic and both primary and secondary biogenic tracers. The atmospheric loading by anthropogenic sources (38%) is dominant compared to biogenic sources (29%). This dominance is likely related to the short lifetime of C_5H_8 and its oxidation products. No marine source was identified from the PMF algorithm, in part due to the omission of DMS data from the analysis. At night, the contribution

515   of mesoscale sources is strongly reduced and the background factor becomes dominant. This diel variability is consistent with the description of mesoscale transport in previous studies (Lesouëf et al., 2011; Baray et al., 2013; Guilpart et al., 2017; Foucart et al., 2018; Duflot et al., 2019). The observatory is located near a horizontal wind shear front between overflowing trade winds coming from the east and the coupled thermally driven sea-breeze with upslope transport during the day (Duflot et al., 2019). A previous study however found that overflowing trade winds were correlated with a reduced influence of surface

520   emissions (Duflot et al., 2019). This is not reproduced here, as overflowing winds coming from the direction of the Maïdo mountain summit during the day were still sensitive to surface emissions. At night however, the cold island surface pulls down FT air masses towards the observatory, limiting the impact of mesoscale surface emissions on the atmospheric composition. This is consistent with known mesoscale transport features (Lesouëf et al., 2011; Baray et al., 2013; Guilpart et al., 2017; Duflot et al., 2019). The interquartile range of nighttime concentrations, characteristic for the free troposphere, of CH_3OH,

525   CH_3CN, CH_3CHO, $HCOOH$, CH_3COCH_3, CH_3COOH and MEK were found to be 525–887 pptv, 79–110 pptv, 61–101 pptv, 172–335 pptv, 259–379 pptv, 64–164 and 11–21 pptv respectively. Combining results from FLEXPART-AROME and the PMF analysis, we identified emissions hotspots with significant impact on the atmospheric composition at the Maïdo observatory. Biogenic emission hotspots identified from both the highest contributions of primary and secondary biogenic source factors revealed a region east of the observatory, together with the "Rivière des Galets" river canyon, as important sources of biogenic

530   tracers recorded at the observatory. The most relevant anthropogenic emission hotspots are located west of the observatory.

Specifically, industrial regions as Le Port and Le Gol, together with the second largest city on the island, Saint-Paul were found to have a large influence on the atmospheric composition at Maïdo. The background/biomass burning source factor from PMF was much less sensitive to surface emissions on the mesoscale compared to other sources.

Data availability. The core hs-PTR-MS dataset is made available online (Amelynck et al., 2021).

535 *Author contributions.* The analysis was conceptualized by C.A., J.B., and B.V. The formal analysis and visualisation was performed by B.V. Data acquisition, quality assurance, and processing of hs-PTR-MS data done by C.A., N.S., and B.V. The PMF analysis and FLEXPART-AROME simulations were performed by B.V. Data management of the meteorological parameters and the PICARRO instrument by C.H. and N.K. The original draft was prepared by B.V. in cooperation with C.A., J.-F.M., T.S., J.B., and N.S. All co-authors were involved in the review and editing process of the final manuscript version.

540 *Competing interests.* The authors declare to have no competing interests.

Acknowledgements. This research was funded by the Belgian Federal Science Policy Office (grant no. BR/175/A2/OCTAVE) and received extra financial support from Horizon 2020 (ACTRIS-2, grant no. 654109). We would like to thank UMS3365 of OSU-Réunion and the technical staff at BIRA-IASB for its support in the deployment of the hs-PTR-MS at Maïdo.

References

545   Amelynck, C., Schoon, N., and Verreyken, B.: Long-Term in Situ (O)VOC Measurements at the Maïdo Observatory (Reunion Island) [Data set], https://doi.org/10.18758/71021061, 2021.

Andreae, M. O.: Emission of Trace Gases and Aerosols from Biomass Burning – an Updated Assessment, Atmospheric Chemistry and Physics, 19, 8523–8546, https://doi.org/10.5194/acp-19-8523-2019, 2019.

Baasandorj, M., Millet, D. B., Hu, L., Mitroo, D., and Williams, B. J.: Measuring Acetic and Formic Acid by Proton-Transfer-Reaction Mass
550   Spectrometry: Sensitivity, Humidity Dependence, and Quantifying Interferences, Atmospheric Measurement Techniques, 8, 1303–1321, https://doi.org/10.5194/amt-8-1303-2015, 2015.

Baldy, S., Ancellet, G., Bessafi, M., Badr, A., and Luk, D. L. S.: Field Observations of the Vertical Distribution of Tropospheric Ozone at the Island of Reunion (Southern Tropics), Journal of Geophysical Research: Atmospheres, 101, 23 835–23 849, https://doi.org/10.1029/95JD02929, 1996.

555   Baray, J.-L., Courcoux, Y., Keckhut, P., Portafaix, T., Tulet, P., Cammas, J.-P., Hauchecorne, A., Godin Beekmann, S., Mazière, M. D., Hermans, C., Desmet, F., Sellegri, K., Colomb, A., Ramonet, M., Sciare, J., Vuillemin, C., Hoareau, C., Dionisi, D., Duflot, V., Vérèmes, H., Porteneuve, J., Gabarrot, F., Gaudo, T., Metzger, J.-M., Payen, G., Leclair de Bellevue, J., Barthe, C., Posny, F., Ricaud, P., Abchiche, A., and Delmas, R.: Maïdo Observatory: A New High-Altitude Station Facility at Reunion Island (21° S, 55° E) for Long-Term Atmospheric Remote Sensing and in Situ Measurements, Atmospheric Measurement Techniques, 6, 2865–2877, https://doi.org/10.5194/amt-6-2865-
560   2013, 2013.

Berglen, T. F.: A Global Model of the Coupled Sulfur/Oxidant Chemistry in the Troposphere: The Sulfur Cycle, Journal of Geophysical Research, 109, D19 310, https://doi.org/10.1029/2003JD003948, 2004.

Bernhammer, A.-K., Breitenlechner, M., Keutsch, F. N., and Hansel, A.: Technical Note: Conversion of Isoprene Hydroxy Hydroperoxides (ISOPOOHs) on Metal Environmental Simulation Chamber Walls, Atmospheric Chemistry and Physics, 17, 4053–4062,
565   https://doi.org/10.5194/acp-17-4053-2017, 2017.

Blake, N. J., Blake, D. R., Wingenter, O. W., Sive, B. C., Kang, C. H., Thornton, D. C., Bandy, A. R., Atlas, E., Flocke, F., Harris, J. M., and Rowland, F. S.: Aircraft Measurements of the Latitudinal, Vertical, and Seasonal Variations of NMHCs, Methyl Nitrate, Methyl Halides, and DMS during the First Aerosol Characterization Experiment (ACE 1), Journal of Geophysical Research: Atmospheres, 104, 21 803–21 817, https://doi.org/10.1029/1999JD900238, 1999.

570   Brioude, J., Arnold, D., Stohl, A., Cassiani, M., Morton, D., Seibert, P., Angevine, W., Evan, S., Dingwell, A., Fast, J. D., Easter, R. C., Pisso, I., Burkhart, J., and Wotawa, G.: The Lagrangian Particle Dispersion Model FLEXPART-WRF Version 3.1, Geoscientific Model Development, 6, 1889–1904, https://doi.org/10.5194/gmd-6-1889-2013, 2013.

Colomb, A., Gros, V., Alvain, S., Sarda-Esteve, R., Bonsang, B., Moulin, C., Klüpfel, T., and Williams, J.: Variation of Atmospheric Volatile Organic Compounds over the Southern Indian Ocean (30–49° S), Environmental Chemistry, 6, 70–82, https://doi.org/10.1071/EN08072,
575   2009.

Crippa, M., Solazzo, E., Huang, G., Guizzardi, D., Koffi, E., Muntean, M., Schieberle, C., Friedrich, R., and Janssens-Maenhout, G.: High Resolution Temporal Profiles in the Emissions Database for Global Atmospheric Research, Scientific Data, 7, 121, https://doi.org/10.1038/s41597-020-0462-2, 2020.

de Gouw, J. A.: Emission Sources and Ocean Uptake of Acetonitrile (CH_3CN) in the Atmosphere, Journal of Geophysical Research, 108,
580   4329, https://doi.org/10.1029/2002JD002897, 2003.

Duflot, V., Dils, B., Baray, J. L., Mazière, M. D., Attié, J. L., Vanhaelewyn, G., Senten, C., Vigouroux, C., Clain, G., and Delmas, R.: Analysis of the Origin of the Distribution of CO in the Subtropical Southern Indian Ocean in 2007, Journal of Geophysical Research: Atmospheres, 115, https://doi.org/10.1029/2010JD013994, 2010.

Duflot, V., Tulet, P., Flores, O., Barthe, C., Colomb, A., Deguillaume, L., Vaïtilingom, M., Perring, A., Huffman, A., Hernandez, M. T., Sellegri, K., Robinson, E., O'Connor, D. J., Gomez, O. M., Burnet, F., Bourrianne, T., Strasberg, D., Rocco, M., Bertram, A. K., Chazette, P., Totems, J., Fournel, J., Stamenoff, P., Metzger, J.-M., Chabasset, M., Rousseau, C., Bourrianne, E., Sancelme, M., Delort, A.-M., Wegener, R. E., Chou, C., and Elizondo, P.: Preliminary Results from the FARCE 2015 Campaign: Multidisciplinary Study of the Forest–Gas–Aerosol–Cloud System on the Tropical Island of La Réunion, Atmospheric Chemistry and Physics, 19, 10 591–10 618, https://doi.org/10.5194/acp-19-10591-2019, 2019.

Dupuy, S., Gaetano, R., and Le Mézo, L.: Mapping Land Cover on Reunion Island in 2017 Using Satellite Imagery and Geospatial Ground Data, Data in Brief, 28, 104 934, https://doi.org/10.1016/j.dib.2019.104934, 2020.

Farmer, D. K. and Riches, M.: Measuring Biosphere–Atmosphere Exchange of Short-Lived Climate Forcers and Their Precursors, Accounts of Chemical Research, 53, 1427–1435, https://doi.org/10.1021/acs.accounts.0c00203, 2020.

Foucart, B., Sellegri, K., Tulet, P., Rose, C., Metzger, J.-M., and Picard, D.: High Occurrence of New Particle Formation Events at the Maïdo High-Altitude Observatory (2150 m), Réunion (Indian Ocean), Atmospheric Chemistry and Physics, 18, 9243–9261, https://doi.org/10.5194/acp-18-9243-2018, 2018.

Fournaise Info: Tableau des éruptions, https://fournaise.info/tableau_eruptions/, last access: 10 December 2020, 2018.

Guenther, A. B., Zimmerman, P. R., Harley, P. C., Monson, R. K., and Fall, R.: Isoprene and Monoterpene Emission Rate Variability: Model Evaluations and Sensitivity Analyses, Journal of Geophysical Research, 98, 12 609, https://doi.org/10.1029/93JD00527, 1993.

Guilpart, E., Vimeux, F., Evan, S., Brioude, J., Metzger, J.-M., Barthe, C., Risi, C., and Cattani, O.: The Isotopic Composition of Near-Surface Water Vapor at the Maïdo Observatory (Reunion Island, Southwestern Indian Ocean) Documents the Controls of the Humidity of the Subtropical Troposphere, Journal of Geophysical Research: Atmospheres, 122, 9628–9650, https://doi.org/10.1002/2017JD026791, 2017.

IPCC: Climate Change 2013: The Physical Science Basis. Contribution of Working Group I to the Fifth Assessment Report of the Intergovernmental Panel on Climate Change, Cambridge University Press, Cambridge, United Kingdom and New York, NY, USA, 2013.

Jardine, K., Yañez-Serrano, A. M., Williams, J., Kunert, N., Jardine, A., Taylor, T., Abrell, L., Artaxo, P., Guenther, A., Hewitt, C. N., House, E., Florentino, A. P., Manzi, A., Higuchi, N., Kesselmeier, J., Behrendt, T., Veres, P. R., Derstroff, B., Fuentes, J. D., Martin, S. T., and Andreae, M. O.: Dimethyl Sulfide in the Amazon Rain Forest: DMS in the Amazon, Global Biogeochemical Cycles, 29, 19–32, https://doi.org/10.1002/2014GB004969, 2015.

Jerrett, M., Burnett, R. T., Pope, C. A., Ito, K., Thurston, G., Krewski, D., Shi, Y., Calle, E., and Thun, M.: Long-Term Ozone Exposure and Mortality, New England Journal of Medicine, 360, 1085–1095, https://doi.org/10.1056/NEJMoa0803894, 2009.

Karl, T., Hansel, A., Märk, T., Lindinger, W., and Hoffmann, D.: Trace Gas Monitoring at the Mauna Loa Baseline Observatory Using Proton-Transfer Reaction Mass Spectrometry, International Journal of Mass Spectrometry, 223-224, 527–538, https://doi.org/10.1016/S1387-3806(02)00874-6, 2003.

Kloster, S., Feichter, J., Maier-Reimer, E., Six, K. D., Stier, P., and Wetzel, P.: DMS Cycle in the Marine Ocean-Atmosphere System – a Global Model Study, Biogeosciences, 3, 29–51, https://doi.org/10.5194/bg-3-29-2006, 2006.

Lac, C., Chaboureau, J.-P., Masson, V., Pinty, J.-P., Tulet, P., Escobar, J., Leriche, M., Barthe, C., Aouizerats, B., Augros, C., Aumond, P., Auguste, F., Bechtold, P., Berthet, S., Bielli, S., Bosseur, F., Caumont, O., Cohard, J.-M., Colin, J., Couvreux, F., Cuxart, J., Delautier,

G., Dauhut, T., Ducrocq, V., Filippi, J.-B., Gazen, D., Geoffroy, O., Gheusi, F., Honnert, R., Lafore, J.-P., Lebeaupin Brossier, C., Libois,
Q., Lunet, T., Mari, C., Maric, T., Mascart, P., Mogé, M., Molinié, G., Nuissier, O., Pantillon, F., Peyrillé, P., Pergaud, J., Perraud, E.,
Pianezze, J., Redelsperger, J.-L., Ricard, D., Richard, E., Riette, S., Rodier, Q., Schoetter, R., Seyfried, L., Stein, J., Suhre, K., Taufour,
M., Thouron, O., Turner, S., Verrelle, A., Vié, B., Visentin, F., Vionnet, V., and Wautelet, P.: Overview of the Meso-NH Model Version
5.4 and Its Applications, Geoscientific Model Development, 11, 1929–1969, https://doi.org/10.5194/gmd-11-1929-2018, 2018.

Lana, A., Bell, T. G., Simó, R., Vallina, S. M., Ballabrera-Poy, J., Kettle, A. J., Dachs, J., Bopp, L., Saltzman, E. S., Stefels, J., Johnson, J. E.,
and Liss, P. S.: An Updated Climatology of Surface Dimethlysulfide Concentrations and Emission Fluxes in the Global Ocean: UPDATED
DMS CLIMATOLOGY, Global Biogeochemical Cycles, 25, n/a–n/a, https://doi.org/10.1029/2010GB003850, 2011.

Le Monde: Gilets jaunes: couvre-feu partiel à La Réunion, bloquée par des barrages routiers, https://www.lemonde.fr/la-reunion/article/
2018/11/20/un-couvre-feu-partiel-instaure-a-la-reunion-bloquee-par-les-gilets-jaunes_5385926_1616695.html, last access: 10 Decem-
ber 2020, 2018.

Lesouëf, D., Gheusi, F., Delmas, R., and Escobar, J.: Numerical Simulations of Local Circulations and Pollution Transport over Reunion
Island, Annales Geophysicae, 29, 53–69, https://doi.org/10.5194/angeo-29-53-2011, 2011.

Liu, Y. J., Herdlinger-Blatt, I., McKinney, K. A., and Martin, S. T.: Production of Methyl Vinyl Ketone and Methacrolein via the Hydroper-
oxyl Pathway of Isoprene Oxidation, Atmospheric Chemistry and Physics, 13, 5715–5730, https://doi.org/10.5194/acp-13-5715-2013,
2013.

Millet, D. B., Guenther, A., Siegel, D. A., Nelson, N. B., Singh, H. B., de Gouw, J. A., Warneke, C., Williams, J., Eerdekens, G.,
Sinha, V., Karl, T., Flocke, F., Apel, E., Riemer, D. D., Palmer, P. I., and Barkley, M.: Global Atmospheric Budget of Acetaldehyde:
3-D Model Analysis and Constraints from in-Situ and Satellite Observations, Atmospheric Chemistry and Physics, 10, 3405–3425,
https://doi.org/10.5194/acp-10-3405-2010, 2010.

Météo France: Archive of Cyclone Seasons - Details of archived systems, http://www.meteo.fr/temps/domtom/La_Reunion/webcmrs9.0/
anglais/index.html, last access: 10 December 2020, 2020.

Norris, G., Duvall, R., Brown, S., and Bai, S.: EPA Postive Matrix Factorization (PMF) 5.0 Fundamentals and User Guide, 2014.

Pernov, J. B., Bossi, R., Lebourgeois, T., Nøjgaard, J. K., Holzinger, R., Hjorth, J. L., and Skov, H.: Atmospheric VOC Measurements at
a High Arctic Site: Characteristics and Source Apportionment, Preprint, Gases/Field Measurements/Troposphere/Chemistry (chemical
composition and reactions), https://doi.org/10.5194/acp-2020-528, 2020.

Pisso, I., Sollum, E., Grythe, H., Kristiansen, N. I., Cassiani, M., Eckhardt, S., Arnold, D., Morton, D., Thompson, R. L., Groot Zwaaftink,
C. D., Evangeliou, N., Sodemann, H., Haimberger, L., Henne, S., Brunner, D., Burkhart, J. F., Fouilloux, A., Brioude, J., Philipp, A.,
Seibert, P., and Stohl, A.: The Lagrangian Particle Dispersion Model FLEXPART Version 10.4, Geoscientific Model Development, 12,
4955–4997, https://doi.org/10.5194/gmd-12-4955-2019, 2019.

Read, K. A., Carpenter, L. J., Arnold, S. R., Beale, R., Nightingale, P. D., Hopkins, J. R., Lewis, A. C., Lee, J. D., Mendes, L., and Pickering,
S. J.: Multiannual Observations of Acetone, Methanol, and Acetaldehyde in Remote Tropical Atlantic Air: Implications for Atmospheric
OVOC Budgets and Oxidative Capacity, Environmental Science & Technology, 46, 11 028–11 039, https://doi.org/10.1021/es302082p,
2012.

Rivera-Rios, J. C., Nguyen, T. B., Crounse, J. D., Jud, W., St. Clair, J. M., Mikoviny, T., Gilman, J. B., Lerner, B. M., Kaiser, J. B., Gouw,
J., Wisthaler, A., Hansel, A., Wennberg, P. O., Seinfeld, J. H., and Keutsch, F. N.: Conversion of Hydroperoxides to Carbonyls in Field
and Laboratory Instrumentation: Observational Bias in Diagnosing Pristine versus Anthropogenically Controlled Atmospheric Chemistry,
Geophysical Research Letters, 41, 8645–8651, https://doi.org/10.1002/2014GL061919, 2014.

Rocco, M., Colomb, A., Baray, J.-L., Amelynck, C., Verreyken, B., Borbon, A., Pichon, J.-M., Bouvier, L., Schoon, N., Gros, V., Sarda-Esteve, R., Tulet, P., Metzger, J.-M., Duflot, V., Guadagno, C., Peris, G., and Brioude, J.: Analysis of Volatile Organic Compounds during the OCTAVE Campaign: Sources and Distributions of Formaldehyde on Reunion Island, Atmosphere, 11, 140, https://doi.org/10.3390/atmos11020140, 2020.

Seibert, P. and Frank, A.: Source-Receptor Matrix Calculation with a Lagrangian Particle Dispersion Model in Backward Mode, Atmospheric Chemistry and Physics, 4, 51–63, https://doi.org/10.5194/acp-4-51-2004, 2004.

Stohl, A., Forster, C., Frank, A., Seibert, P., and Wotawa, G.: Technical Note: The Lagrangian Particle Dispersion Model FLEXPART Version 6.2, Atmospheric Chemistry and Physics, 5, 2461–2474, https://doi.org/10.5194/acp-5-2461-2005, 2005.

Travis, K. R., Heald, C. L., Allen, H. M., Apel, E. C., Arnold, S. R., Blake, D. R., Brune, W. H., Chen, X., Commane, R., Crounse, J. D., Daube, B. C., Diskin, G. S., Elkins, J. W., Evans, M. J., Hall, S. R., Hintsa, E. J., Hornbrook, R. S., Kasibhatla, P. S., Kim, M. J., Luo, G., McKain, K., Millet, D. B., Moore, F. L., Peischl, J., Ryerson, T. B., Sherwen, T., Thames, A. B., Ullmann, K., Wang, X., Wennberg, P. O., Wolfe, G. M., and Yu, F.: Constraining Remote Oxidation Capacity with ATom Observations, Atmospheric Chemistry and Physics, 20, 7753–7781, https://doi.org/10.5194/acp-20-7753-2020, 2020.

Tulet, P., Muro, A. D., Colomb, A., Denjean, C., Duflot, V., Arellano, S., Foucart, B., Brioude, J., Sellegri, K., Peltier, A., Aiuppa, A., Barthe, C., Bhugwant, C., Bielli, S., Boissier, P., Boudoire, G., Bourrianne, T., Brunet, C., Burnet, F., Cammas, J.-P., Gabarrot, F., Galle, B., Giudice, G., Guadagno, C., Jeamblu, F., Kowalski, P., Leclair de Bellevue, J., Marquestaut, N., Mékies, D., Metzger, J.-M., Pianezze, J., Portafaix, T., Sciare, J., Tournigand, A., and Villeneuve, N.: First Results of the Piton de La Fournaise STRAP 2015 Experiment: Multidisciplinary Tracking of a Volcanic Gas and Aerosol Plume, Atmospheric Chemistry and Physics, 17, 5355–5378, https://doi.org/10.5194/acp-17-5355-2017, 2017.

Verreyken, B., Brioude, J., and Evan, S.: Development of Turbulent Scheme in the FLEXPART-AROME v1.2.1 Lagrangian Particle Dispersion Model, Geoscientific Model Development, 12, 4245–4259, https://doi.org/10.5194/gmd-12-4245-2019, 2019.

Verreyken, B., Amelynck, C., Brioude, J., Müller, J.-F., Schoon, N., Kumps, N., Colomb, A., Metzger, J.-M., Lee, C. F., Koenig, T. K., Volkamer, R., and Stavrakou, T.: Characterisation of African Biomass Burning Plumes and Impacts on the Atmospheric Composition over the South-West Indian Ocean, Atmospheric Chemistry and Physics, 20, 14 821–14 845, https://doi.org/10.5194/acp-20-14821-2020, 2020.

Vettikkat, L., Sinha, V., Datta, S., Kumar, A., Hakkim, H., Yadav, P., and Sinha, B.: Significant Emissions of Dimethyl Sulfide and Monoterpenes by Big-Leaf Mahogany Trees: Discovery of a Missing Dimethyl Sulfide Source to the Atmospheric Environment, Atmospheric Chemistry and Physics, 20, 375–389, https://doi.org/10.5194/acp-20-375-2020, 2020.

Vigouroux, C., Stavrakou, T., Whaley, C., Dils, B., Duflot, V., Hermans, C., Kumps, N., Metzger, J.-M., Scolas, F., Vanhaelewyn, G., Müller, J.-F., Jones, D. B. A., Li, Q., and Mazière, M. D.: FTIR Time-Series of Biomass Burning Products (HCN, C_2H_6, C_2H_2, CH_3OH, and HCOOH) at Reunion Island (21° S, 55° E) and Comparisons with Model Data, Atmospheric Chemistry and Physics, 12, 10 367–10 385, https://doi.org/10.5194/acp-12-10367-2012, 2012.

Wennberg, P. O., Bates, K. H., Crounse, J. D., Dodson, L. G., McVay, R. C., Mertens, L. A., Nguyen, T. B., Praske, E., Schwantes, R. H., Smarte, M. D., Clair, J. M. S., Teng, A. P., Zhang, X., and Seinfeld, J. H.: Gas-Phase Reactions of Isoprene and Its Major Oxidation Products, Chemical Reviews, https://doi.org/10.1021/acs.chemrev.7b00439, 2018.

Yang, M., Blomquist, B. W., and Nightingale, P. D.: Air-Sea Exchange of Methanol and Acetone during HiWinGS: Estimation of Air Phase, Water Phase Gas Transfer Velocities, Journal of Geophysical Research: Oceans, 119, 7308–7323, https://doi.org/10.1002/2014JC010227, 2014.

Zhao, Y., Saunois, M., Bousquet, P., Lin, X., Berchet, A., Hegglin, M. I., Canadell, J. G., Jackson, R. B., Hauglustaine, D. A., Szopa, S.,
695   Stavert, A. R., Abraham, N. L., Archibald, A. T., Bekki, S., Deushi, M., Jöckel, P., Josse, B., Kinnison, D., Kirner, O., Marécal, V.,
       O'Connor, F. M., Plummer, D. A., Revell, L. E., Rozanov, E., Stenke, A., Strode, S., Tilmes, S., Dlugokencky, E. J., and Zheng, B.:
       Inter-Model Comparison of Global Hydroxyl Radical (OH) Distributions and Their Impact on Atmospheric Methane over the 2000–2016
       Period, Atmospheric Chemistry and Physics, 19, 13 701–13 723, https://doi.org/10.5194/acp-19-13701-2019, 2019.